

Computational prediction of probabilistic ignition threshold of pressed granular Octahydro-1,3,5,7-tetranitro-1,3,5,7-tetrazocine (HMX) under shock loading

Seokpum Kim, Christopher Miller, Yasuyuki Horie, Christopher Molek, Eric Welle, and Min Zhou

Citation: [Journal of Applied Physics](#) **120**, 115902 (2016); doi: 10.1063/1.4962211

View online: <http://dx.doi.org/10.1063/1.4962211>

View Table of Contents: <http://scitation.aip.org/content/aip/journal/jap/120/11?ver=pdfcov>

Published by the [AIP Publishing](#)

Articles you may be interested in

[A molecular dynamics study of the early-time mechanical heating in shock-loaded octahydro-1,3,5,7-tetranitro-1,3,5,7-tetrazocine-based explosives](#)

[J. Appl. Phys.](#) **116**, 033516 (2014); 10.1063/1.4890715

[Initial chemical events in shocked octahydro-1,3,5,7-tetranitro-1,3,5,7-tetrazocine: A new initiation decomposition mechanism](#)

[J. Chem. Phys.](#) **136**, 044516 (2012); 10.1063/1.3679384

[On the low pressure shock initiation of octahydro-1,3,5,7-tetranitro-1,3,5,7-tetrazocine based plastic bonded explosives](#)

[J. Appl. Phys.](#) **107**, 094906 (2010); 10.1063/1.3407570

[Quantitative analysis of damage in an octahydro-1,3,5,7-tetranitro-1,3,5,7-tetrazocine-based composite explosive subjected to a linear thermal gradient](#)

[J. Appl. Phys.](#) **97**, 093507 (2005); 10.1063/1.1879072

[An estimate of the linear strain rate dependence of octahydro-1,3,5,7-tetranitro-1,3,5,7-tetrazocine](#)

[J. Appl. Phys.](#) **86**, 6717 (1999); 10.1063/1.371722

Computational prediction of probabilistic ignition threshold of pressed granular Octahydro-1,3,5,7-tetranitro-1,3,5,7-tetrazocine (HMX) under shock loading

Seokpum Kim,¹ Christopher Miller,¹ Yasuyuki Horie,² Christopher Molek,³ Eric Welle,³ and Min Zhou^{1,a)}

¹The George W. Woodruff School of Mechanical Engineering, School of Materials Science and Engineering, Georgia Institute of Technology, Atlanta, Georgia 30332-0405, USA

²(ret.) Air Force Research Lab, Munitions Directorate, 2306 Perimeter Road, Eglin AFB, Florida 32542, USA

³Air Force Research Lab, Munitions Directorate, 2306 Perimeter Road, Eglin AFB, Florida 32542, USA

(Received 15 March 2016; accepted 23 August 2016; published online 19 September 2016; corrected 1 November 2016)

The probabilistic ignition thresholds of pressed granular Octahydro-1,3,5,7-tetranitro-1,3,5,7-tetrazocine explosives with average grain sizes between 70 μm and 220 μm are computationally predicted. The prediction uses material microstructure and basic constituent properties and does not involve curve fitting with respect to or prior knowledge of the attributes being predicted. The specific thresholds predicted are James-type relations between the energy flux and energy fluence for given probabilities of ignition. Statistically similar microstructure sample sets are computationally generated and used based on the features of micrographs of materials used in actual experiments. The predicted thresholds are in general agreement with measurements from shock experiments in terms of trends. In particular, it is found that grain size significantly affects the ignition sensitivity of the materials, with smaller sizes leading to lower energy thresholds required for ignition. For example, 50% ignition threshold of the material with an average grain size of 220 μm is approximately 1.4–1.6 times that of the material with an average grain size of 70 μm in terms of energy fluence. The simulations account for the controlled loading of thin-flyer shock experiments with flyer velocities between 1.5 and 4.0 km/s, constituent elasto-viscoplasticity, fracture, post-fracture contact and friction along interfaces, bulk inelastic heating, interfacial frictional heating, and heat conduction. The constitutive behavior of the materials is described using a finite deformation elasto-viscoplastic formulation and the Birch-Murnaghan equation of state. The ignition thresholds are determined via an explicit analysis of the size and temperature states of hotspots in the materials and a hotspot-based ignition criterion. The overall ignition threshold analysis and the microstructure-level hotspot analysis also lead to the definition of a macroscopic ignition parameter (J) and a microscopic ignition risk parameter (R) which are statistically related. The relationships between these parameters are established and delineated. *Published by AIP Publishing.* [<http://dx.doi.org/10.1063/1.4962211>]

I. INTRODUCTION

The subject of ignition (go or no-go) occupies a central place in consideration of explosives' safety and performance. As a result, there exists a large body of literature covering a wide range of scenarios, from loading and environment, spatial and time scales, to material composition and microstructure. In particular, the establishment of precise conditions for the ignition of real energetic materials is especially important. The threshold conditions are commonly expressed by simple analytic functions. Solov'ev¹ reviewed several such thresholds, each of which focuses on a different initiation mechanism. One of the newer and most commonly used thresholds is the James relation.² This threshold is chosen in this study not only because it accurately describes experimental data but also because it considers two macroscopic state variables, one is the rate at which energy is imparted to a sample (energy flux) and the other is the total energy imparted to a sample (energy fluence). So far, the

establishment of ignition thresholds has been exclusively an experimental endeavor. In this paper, we report the development of a method for predicting the James type ignition thresholds through microstructural level simulations and the result of applying this method to a real explosive system. The method is an extension of a novel computational capability based on the Lagrangian cohesive finite element method (CFEM) and represents a pathway toward building predictive tools for evaluating and comparing solid explosives at the grain scale and for establishing relations between macroscopic safety/performance and microscopic structures of the materials. The method and the relations it yields are such that they can be used in the design of new explosives via heuristic improvement of performance through microstructural, constituent, and compositional engineering. In the pursuit of this objective here, emphasis is placed on (1) quantification of conditions of ignition under well-understood planar shock wave stimuli typically applied in experiments, (2) capture of essential material attributes and physical processes that control ignition, (3) recognition of the probabilistic nature of the ignition phenomenon, and (4) comparison with independent experimental measurements.

^{a)}Author to whom correspondence should be addressed. Electronic mail: min.zhou@gatech.edu

Due to the fact that material heterogeneity is one of the most important sources of stochasticity in material behavior, the quantification of the statistical variations of material attributes at the microstructural level, such as grain shape and size distributions, is essential in the discussion of reliability-based design of energetic materials and in the determination of the ignition probability under given stimuli that lead to violent reactions. Despite this, the stochasticity of ignition thresholds, especially the influence of microstructural variations of material attributes, such as grain size distributions and defects, has not been systematically studied.^{3,4} In this study, this issue is addressed in a manner that is consistent with experimental quantification of uncertainty via the generation and use of multiple statistically similar samples of each material design setting.

Broadly speaking, the modeling of shock ignition at the mesoscale level is typically carried out as a part of modeling shock-to-detonation transition (SDT). There are two approaches, depending on whether hotspots are explicitly treated or not. In the literature, the phrase “shock initiation” is often used to emphasize the transition to detonation.⁵ The first approach involves treating hotspots explicitly based on a chosen mechanism of energy localization⁶ (e.g., predominantly plastic pore collapse). The second approach does not involve treating hotspots explicitly, instead ignition is treated via a numerical switch to a burn model (rate law) in large-scale engineering calculations.⁷ Both approaches have two basic features. The first is an assumption on the internal energy function (equation of state (EOS)). The most common is a mass-weighted sum of constituent internal energies which contains the fraction of reacted explosive mass (called progress variable) and heat release from chemical reaction. The second is the rate law that controls the evolution of “burn” via the progress variable. This second approach does not describe the mechanisms of ignition or hotspot evolution. However, it is known that these burn models can be calibrated to match 50% threshold sensitivity of high explosives.⁴

The CFEM capability used in this study does not treat the SDT transition and focuses instead on hotspot evolution and the criticality condition for thermal runaway. Studies emphasizing the SDT transition and studies focusing on the processes leading up to and the attainment of thermal runaway (which ultimately lead to the SDT transition) are parallel and mutually reinforcing. Thermal runaway studies allow ignition thresholds to be established (focus of this paper) and can provide input for SDT analyses. The evolution of hotspots has been studied by many researchers.^{6,8–10} For example, Bennett *et al.*⁸ proposed a model for hotspots generated by random cracks and associated friction. Benson and Conley⁹ used Eulerian FEM simulations to study hotspots generated by plastic and viscous dissipation. Austin *et al.*¹¹ used the ALE3D framework to study the reaction in hotspots at a pore, accounting for crystallographic slip. Frictional dissipation is one of the main hotspot formation mechanisms. Chaudhri¹² observed the reaction front in β -lead azide using a high-speed camera, and found that reaction-generated stress wave induces new reaction sites ahead of an existing reaction front, and the new reaction is caused by frictional dissipation. Browning and Scammon¹³ established an

ignition model based on inter-granular frictional dissipation, chemical kinetics, and heat transfer, and obtained the time to ignition and velocities required for reaction. Gruau *et al.*¹⁴ performed the computational analyses of impact tests on polymer-bonded explosives (PBX). In their numerical model, frictional heating is assumed to depend on the macroscopic pressure and plastic shear strain rate. Their study showed that frictional dissipation leads to ignition. Curtis *et al.*¹⁵ used a similar test configuration as Gruau *et al.*¹⁴ (Steven Test) in their numerical study, and found that friction substantially affects the ignition behavior. In our study, the CFEM framework explicitly tracks the arbitrary fracture and post-fracture contact and friction, and captures hotspots generated by various dissipation mechanisms including friction, viscoelasticity, viscoplasticity, and heat conduction. Specifically, in Refs. 16–18, we analyzed the energy dissipation in PBX and observed that frictional dissipation is the dominant heating mechanism. The criticality condition for thermal explosion is identified as the ignition thresholds (boundaries between go and no-go). The justification for this assumption is based on the careful analysis of in-material gauge records of Octahydro-1,3,5,7-tetranitro-1,3,5,7-tetrazocine (HMX) and triaminotrinitrobenzene or 2,4,6-triamino-1,3,5-trinitrobenzene (TATB) based explosives by James and Lambourn.¹⁹ They showed that the reaction (behind the shock wave front) is a function of shock strength and time along the particle path, and is independent of local flow variables behind the shock such as pressure and temperature. In other words, “the growth in the pressure or temperature fields does not feed back to the reaction rate.” This observation is fundamental to the present study because it implies that the criticality of hotspots in the sense of thermal explosion²⁰ directly correlates to the initiation of detonation. It also implies that the collective behavior of hotspots may influence the time to detonation, but may not affect the minimum shock threshold condition for initiating detonation, at least to first order. However, the role of distributed hotspots on the go-no-go criticality is not yet well understood.²¹ Based on the observations above, we assume that there is a one-to-one correlation between the existence of critical hotspots which lead to local thermal runaway and the occurrence of eventual detonation. In this paper, we do not consider the issue of subsequent burn after initiation and the time needed to reach detonation. Although these are important issues by themselves, they are topics for separate studies.

The remaining paper consists of three parts. The first part describes the computational framework used to study shock ignition and includes discussion on microstructure representation, loading configuration, and constitutive relations. The second part discusses the simulation results with a focus on shock ignition thresholds in terms of the modified James function and a probabilistic quantification of the thresholds. We then introduce a normalized hotspot temperature as a measure for the ignition risk of individual hotspots [referred to as the hotspot ignition risk determinant (HIRD) or R]. The third part focuses on the major findings, which include predicted James type ignition thresholds for pressed HMX powders, the effect of particle size on the James ignition thresholds, comparison with experimental measurements, and the probability

distribution of the thresholds as a function of the James number (J) as introduced by Gresshoff and Hrousis.⁴

II. FRAMEWORK OF ANALYSIS

Sections II A–II D outline the material properties, loading conditions, constitutive models, and critical hotspot-based criterion. The main assumptions and limitations of these models are discussed in Section II E.

A. Material

The materials are pressed granular HMX with microstructures consisting of HMX grains without binder. In the experiments, materials with different grain sizes are referred to as different “classes.” Of particular interest are Class 3, which has an average grain size of $d_{avg} = 358 \mu\text{m}$, and Class 5, which has an average grain size of $d_{avg} = 6.7 \mu\text{m}$ initially. These HMX grains are then pressed, causing the grain sizes to become somewhat smaller than their original sizes (see Fig. 4 in Ref. 22) due to fracture. Both classes have a density that is 94% the theoretical maximum density (TMD). Figure 1 shows the scanning electron microscope (SEM) images of the microstructures of these two classes of HMX. A small number of abnormally large grains (referred to as “boulders”) are present in the Class 5 material. Samples prepared for shocked experiments are cylindrical pellets with a diameter of 0.5 in. and a height of 0.5 in.

The materials and the experimental procedure of Welle *et al.*²³ serve as a basis and starting point for the computational analysis. In the experiments, multiple samples for each material class and load condition are tested to quantify the ignition threshold distribution. Similarly, for systematic computational quantification of the probabilistic ignition behavior, statistically similar sample sets with multiple (5) samples are computationally generated and tested under identical loading conditions. The computationally generated microstructures mimic the attributes of the experimental

microstructures. The generation uses the 2D Voronoi tessellation.²⁴ The computationally generated samples are designed to achieve two objectives: (1) maintain statistical consistency among samples for each material setting (e.g., consistency in grain size distributions, grain volume fraction, and grain shapes for a given average grain size) and (2) focus on trends in key microstructure attribute (grain size) among the different classes of materials. To this end, each sample set follows a mono-modal grain size distribution with a specific average grain size that lies between the average grain sizes of Class 3 and Class 5. This approach allows primary trends in material behavior-microstructure relations to be identified and quantified, while a significant degree of similitude is maintained between the experiments and simulations for a relative comparison.

The grains generated by the Voronoi tessellation have random, multifaceted surfaces interlocking with each other. Yan-Qing and Feng-Lei²⁵ showed that simulations of Brazilian compression of PBX using microstructures generated with this approach match the experiments reasonably well. In our analysis, since frictional dissipation along crack faces under compression is an important mechanism for hotspot generation, the Voronoi tessellation method for generating microstructures is preferred to ensure well-defined intergranular interfaces. This method also allows for the generation of large numbers of microstructures with random variations in morphology and a high-degree of statistical similitude in microstructure attributes, such as grain shape and grain size distributions.

The differences between the experimental samples and computationally generated samples are as follows. First, the large “boulders” in the Class 5 experimental samples are not considered in the computationally generated microstructures, as their percentage is small (<10%) and accounting for such large grains would require much larger representative volumes which are computationally prohibitive for the large number of statistical calculations pursued here. The second

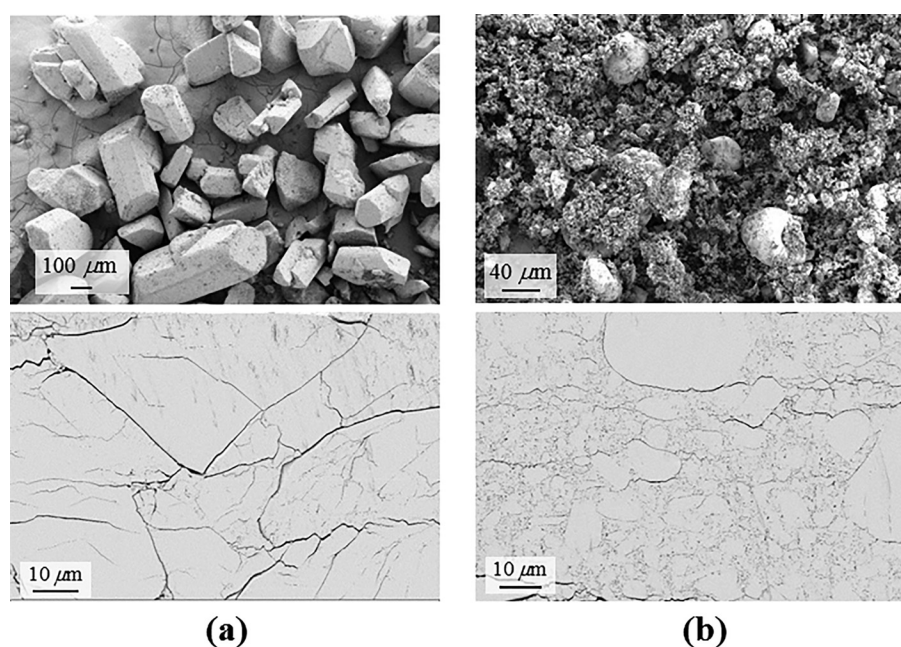


FIG. 1. SEM images of materials used in experiments: (a) Class 3 HMX and (b) Class 5 HMX. Images in the upper row show HMX crystals and images in the lower row show the microstructures made out of the corresponding HMX Classes after pressing. The images are provided courtesy of R. R. Wixom at Sandia National Laboratories.

difference between the experimental samples and computationally generated samples is that the experimental samples have a density that is 94% of the TMD, and more importantly, the voids are too small (Ref. 26) to be resolved explicitly via finite element meshing at the overall size scale of samples analyzed. Therefore, a phenomenological approach for accounting for the effects of voids is taken in the simulations. Specifically, the effects of the voids are considered through variations in the bulk properties of the grains based on the fact that small-scale voids weaken the stiffness and strength of materials. This treatment applies to heterogeneous characteristics including micro and nano scale voids, microcracks, variations in material properties of the HMX grains, and directionality of constituent behavior due to crystalline anisotropy. Here, these heterogeneities are phenomenologically accounted for in a unified manner via random variations in the elastic modulus of the grains. Researchers have analyzed the variations of the elastic moduli due to various factors including defects through experiments and computation. Yang *et al.*²⁷ performed a MD simulation of a copper plate with a void and found that the elastic modulus decreases as the volume fraction of the void increases. Hudson *et al.*^{28,29} quantified the voids in 1,3,5-trinitroperhydro-1,3,5-triazine (RDX) crystals and assigned a defect score to each grain. By using nano-indentation, they measured the elastic modulus and found that the grains with more defects (high defect scores) have a lower elastic modulus. These findings provide justification and serve as a guide for the use of varying elastic modulus values of HMX to phenomenologically account for heterogeneities in the microstructures we analyze. Three levels of elastic modulus ($E = 30.3, 20.0,$ and 12.9 GPa) are randomly assigned to the HMX grains. These levels are determined based on a study of the anisotropy of the elastic behavior of HMX and data in the literature on how voids affect elastic moduli. Specifically, the maximum and minimum values of the Young's modulus of HMX are determined from the stiffness tensor provided by Sewell *et al.*³⁰ The intermediate value is taken to be the Voigt-Ruess-Hill (VRH) average of the stiffness tensor. A similar case has been studied by Dimas *et al.*³¹ who randomly distribute the Young's modulus in the microstructure. The random variations in their study follow a lognormal distribution, with the mean value representing the effective modulus of the simplified homogeneous material. Similarly, in our study, the effective modulus corresponds to the VRH average ($E = 20.0$ GPa) of the stiffness tensor. The grains with the high level of Young's modulus ($E = 30.3$ GPa) are assumed to lie in orientations that have the highest stiffness. The high level of bulk modulus of these grains represents ideal crystals without voids or defects. The grains with the low level of Young's modulus ($E = 12.9$ GPa) are assumed to lie in an orientation that have a lower stiffness. The low level of bulk modulus of these grains represents the crystals with significant amounts of voids or defects. A parametric study is carried out with further variations from these values. It is found that the changes do not have a significant influence on the ignition behavior of the materials. Part of the reason lies in the fact that heating is primarily an outcome of fracture and inelasticity (see Fig. 28 in Ref. 32). We suspect

that the effect of modulus inhomogeneity is indirect through perturbing the fields and inducing fracture and inelastic deformation. Isotropic constitutive relations are implemented in our framework. Anisotropy in the Young's modulus provides a guideline for choosing maximum and minimum values for the isotropic model. Specifically, the maximum and minimum bulk modulus and shear modulus values used differ by the same ratio as the maximum and minimum values of the Young's modulus described above. Although the computationally generated microstructures are not "exact" representations or reproductions of the experimental samples, major attributes are captured, allowing trends in the effects of grain size on ignition behavior to be delineated. It is worth pointing out that what is pursued here is not meant to be an "all-inclusive" effort that explicitly accounts for all possible effects of microstructure on the ignition of the materials. Rather, it is meant to be a novel effort aimed at the computational prediction of ignition thresholds, explicitly accounting for major dissipation mechanisms other than heating due to voids. The consideration of the effects of voids can be carried out in future analyses. Those calculations will involve explicit resolution of small-scale defects and clustering of grain sizes.

The average grain size of the experimental samples for Class 3 ($d_{avg} = 358 \mu\text{m}$) is around 50 times larger than the average grain size of Class 5 ($d_{avg} = 6.7 \mu\text{m}$). Since larger grains require a proportionally larger sample size or representative volume element (RVE), to resolve the large Class 3 grain size with the same fine mesh resolution as required for the small Class 5 grain size, computational models with an extremely large number of degrees of freedom (DoF) would be needed. To keep the overall DoF at a reasonable level for the large number of statistical runs, we take a parametric approach, focusing on the trend in the size effect rather than the absolute sizes. Specifically, we consider the average grain sizes in the range of $d_{avg} = 70\text{--}220 \mu\text{m}$, which lie between the sizes of the Class 3 and Class 5 HMX. The resulting microstructural domain of each sample is 3×6 mm. Although the computationally generated samples have much smaller domain size than the size of experimental samples, the size of 3 mm of the computational samples is at least one order of magnitude larger than the length scale of the largest average grain size ($d_{avg} = 220 \mu\text{m}$) considered, giving sufficient volumetric representation of the microstructures. Liu³³ reported the minimum size of the RVE to be 1.5 mm for a sample with an average grain size of $125 \mu\text{m}$. His finding supports our choice of sample size here for the range of grain sizes considered. Indeed, we have shown that the stress-strain behavior predicted with the current choice of domain size (3 mm) matches the experimental measurements, as seen in Fig. 10 of Ref. 34. In addition, as it will be clarified in Sec. III A, the height of 6 mm is long enough so that the stress attenuates significantly when it reaches the bottom of the domain, such that the ignition is determined by material events near the impact face and materials and boundaries far away from the impact face have no influence on the ignition outcome under the conditions considered here.

Three sets of microstructures are generated with average grain sizes of $d_{avg} = 70, 130,$ and $220 \mu\text{m}$, respectively. Each

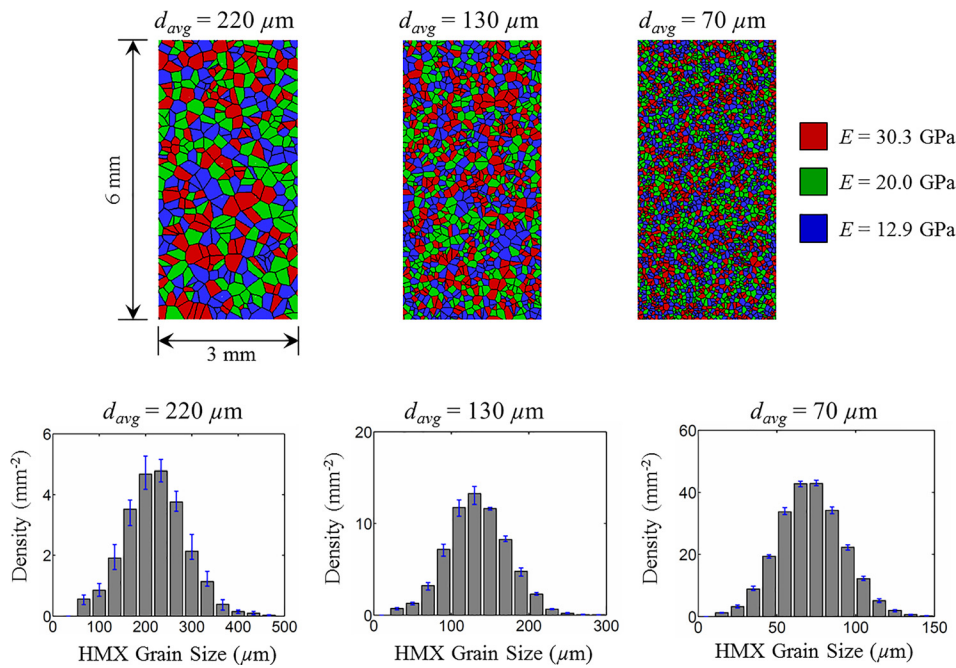


FIG. 2. Computationally generated microstructures and the size distributions of HMX grains in the microstructures for $d_{avg} = 70, 130,$ and $220 \mu\text{m}$. Each microstructure image shown represents one sample in a set of five statistically similar samples which are random instantiations of the same microstructure conditions.

set consists of five samples which have statistically the same attributes in terms of grain size distribution and specific grain boundary surface area. In total, 15 samples (3 sizes \times 5 samples for each size) are generated and used. The microstructure sets and the corresponding grain size distributions are shown in Fig. 2. To illustrate the random variations in microstructure morphology within a particular microstructure set, Figure 3 shows five samples having the same average grain size of $d_{avg} = 220 \mu\text{m}$.

The HMX grains of the samples in the experiments are simply pressed mechanically, leading to very weak or no bonding along the grain boundaries. In the simulations, the bonding strength along the grain boundaries is assumed to be zero.

B. Loading configuration

The shock experiments carried out use an Electric Gun to launch thin flyers, generating a planar shockwave in the HMX samples.²³ Each sample is placed in a steel cup that only allows one face to be exposed to receive the flyer impact. The samples are subjected to shock loading with various combinations of pulse intensities and durations (as determined by the velocity and thickness of the flyer,

respectively). Four different flyer thicknesses ranging from $23 \mu\text{m}$ to $183 \mu\text{m}$ are used. For each flyer thickness (corresponding to a specific pulse duration), different shots with different flyer velocities are conducted on the same material. The ignition response of a sample is recorded as “go” if the sample explodes and as “no go” if the sample does not explode. The results of the experiments are plotted in Figs. 4(a) and 4(b).

The simulations emulate the experiments directly. The computationally generated specimens are initially stress-free and at rest. Impact loading is effected by applying a prescribed boundary velocity at the impact face (top boundary of the sample), as shown in Fig. 5(a). The left and right boundaries are constrained such that lateral expansion does not occur. This confinement mimics the effect of the steel cup holding the experimental sample. This is a 2D model and the conditions of plane-strain prevail. This configuration approximates the shock pulse loading of a sample driven by a thin flyer under the conditions of approximate macroscopic uniaxial strain. The pulse intensity and duration are chosen to correspond to the loading characteristics in the experiments. The experiment conditions and relevant parameters are given in Table I. The imposed velocity at the top boundary (U_p) of the sample is determined by the ratio between the

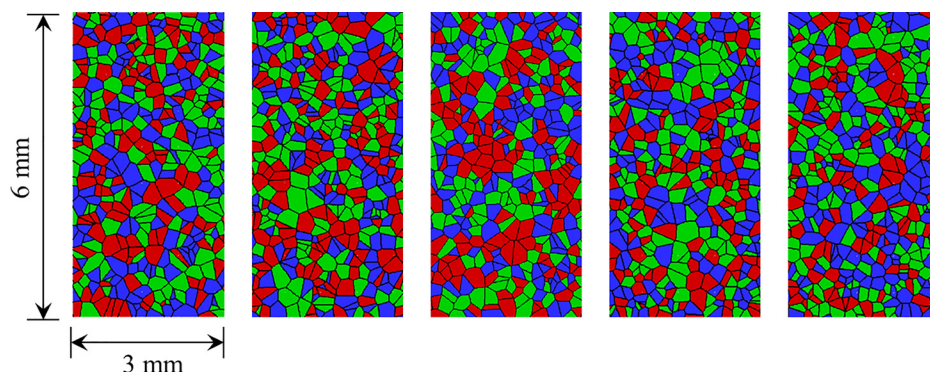


FIG. 3. Multiple samples of computationally generated, statistically similar microstructures with the average grain size of $d_{avg} = 220 \mu\text{m}$.

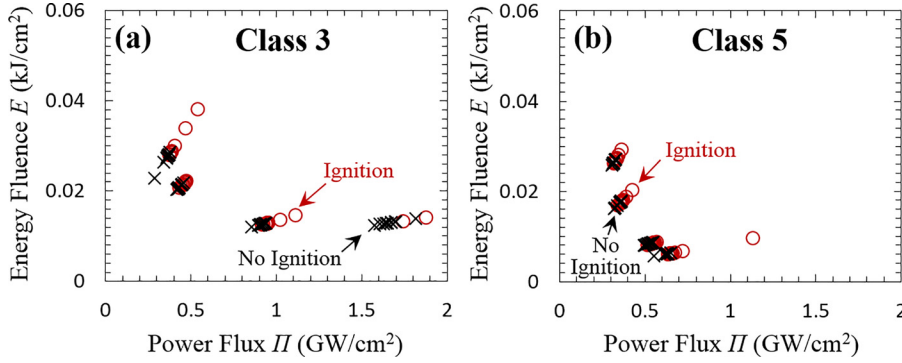


FIG. 4. Ignition threshold determination from experiments using multiple samples of a material with different flyer velocities at each flyer thickness (or pulse duration): (a) Class 3 and (b) Class 5.

longitudinal wave impedances (ρc) of the flyer and the HMX sample as

$$U_p = \frac{\rho_{fly} c_{fly}}{\rho_{fly} c_{fly} + \rho_{HMX} c_{HMX}} V_{fly}, \quad (1)$$

where ρ_{fly} is the density of the flyer, c_{fly} is the wave speed in the flyer, ρ_{HMX} is the density of HMX, c_{HMX} is the wave speed of HMX, and V_{fly} is the launching velocity of the flyer. The range of loading analyzed in the experiment corresponds to the imposed particle velocity range of $U_p = 500 - 1200$ m/s (approximate flyer velocity range of 1.5–4 km/s) and the range of pulse duration of $\tau = 20 - 130$ ns. The specific particle velocity levels considered in the computational analysis are $U_p = 500, 700, 900,$ and 1200 m/s, and the range of pulse duration analyzed is $\tau = 10 - 280$ ns. The pulse duration increment between successive durations depends on the load intensity and varies between $\Delta\tau = 1 - 12$ ns, as listed in Table II. The pulse duration is the time it takes the longitudinal wave to traverse a round trip in the flyer. For each velocity and sample, 10 different pulse durations are considered, yielding 600 microstructure-loading combinations (4 velocities \times 10 pulse durations \times 3 grain sizes \times 5 microstructures). The profile of the imposed shock pulse at the boundary is shown in Fig. 5(b). The velocity rapidly increases from zero to the particle velocity of U_p during the ramp time of $t_{ramp} = 10$ ns. This velocity is kept constant until the pulse time τ is reached. After the pulse time ($t \geq \tau$), the top boundary is released and no external loading is applied, while the boundaries on the left, right, and the bottom remain

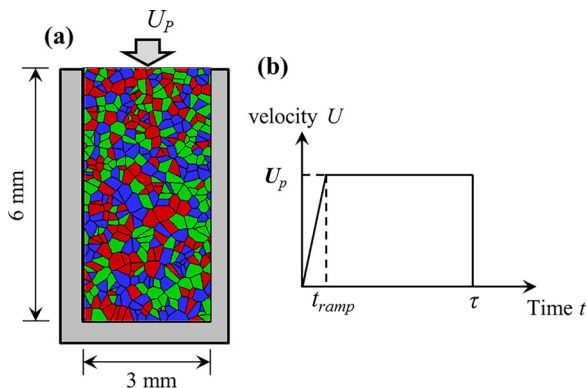


FIG. 5. (a) Configuration of computational model of shock experiments, loading, and boundary conditions considered, and (b) load history imposed on the top boundary of the domain.

constrained in their normal directions. The computational prediction of the “go” and “no go” threshold in this paper follows the same procedure as used in the experiments of Figs. 4(a) and 4(b). As an example of the results, the “go” and “no go” thresholds from each microstructure of grain sizes of 70–220 μm are plotted in Figs. 6(a)–6(c). The symbols represent either “go” or “no-go” for each combination of flyer velocity and pulse duration. The data points are along the vertical lines in Fig. 6 because the simulations are performed for different pulse durations at each flyer velocity which determines the energy flux. On the other hand, experiments are performed at different flyer velocities for each flyer thickness which determines pulse duration, resulting in the data points to line up along the diagonal lines in the energy fluence-power flux space. This slight difference in how the computational and experimental data points populate the domain of analysis does not affect comparison of the two data sets in any way. A total of five microstructures for each grain size are used for the computational analysis, and Figs. 6(a)–6(c) show the results from only one microstructure of each grain size. Details of the computational approach and models are given in Sections II C and II D.

C. Constitutive relations

The simulations are performed using a recently developed Lagrangian cohesive finite element framework.^{17,24,34,35} This framework allows quantification of the effects of microstructure and thermal-mechanical processes, including bulk deformation, interfacial debonding, fracture of grains, and subsequent frictional heating. The constitutive relations for the grains are those of a hydrostatic stress-dependent elasto-viscoplastic material. Specifically, the deviatoric part of the stress tensor carried by the material follows an elasto-viscoplastic constitutive law, and the hydrostatic part of the stress tensor carried by the material follows the Birch-Murnaghan equation of state (B-M EOS).

TABLE I. Material properties of flyer and specimen and conditions of experiments.

Parameters		Flyer 1	Flyer 2	Specimen
Material properties	Longitudinal wave	Parylene-C ⁶⁵	Kapton ⁶⁵	HMX
	Speed c (m/s)	2228	2741	3750
	Density ρ (kg/m ³)	1286	1.414	1910
Experimental condition	Flyer velocity v_{fly}	2–4.2 km/s	1.5–2 km/s	Stationary
	Thickness H	23–37 μm	111–183 μm	12.7 mm

TABLE II. Load conditions and load increments analyzed.

U_p (m/s)	500	700	900	1200
$P \cdot U_p$ (GW/cm ²)	0.173	0.366	0.65	1.273
Range of E (kJ/cm ²)	0.0169–0.0507	0.0132–0.0416	0.0094–0.042	0.0045–0.0429
Range of pulse duration τ (ns)	100–280	40–112	20–65	10–34
minimum τ interval (ns)	12	6	3	1

The term “pressure” and the variable “ P ” refer to the hydrostatic part of the stress in the following discussion. Additionally, an artificial viscosity model for numerical stability is used in association with the EOS. A bi-linear traction-separation model is used for the cohesive elements to account for normal and tangential separations and fracture in grains. Details of the cohesive models and the parameters for transgranular separations are given in Ref. 34. The cohesive strength at the grain-grain interfaces is set to zero. A contact detection algorithm and a subsequent contact force model are used for surfaces after fracture. The Coulomb friction damping model is used for surface elements that are in contact. The coefficient of friction is 0.5 at the contact points between initially debonded surfaces as well as surfaces newly generated as a result of transgranular fracture. Although the coefficient of sliding friction is usually lower than the coefficient of static friction, the same value of 0.5 is used for both for the lack of measured data. The value chosen is based on the work of Green *et al.*³⁶ who reported the range of 0.3–0.7 for PBX 9404. Dickson *et al.*³⁷ reported that the frictional coefficient for PBX 9501 is between 0.4 and 0.5. Chidester *et al.*³⁸ used a value of 0.5 for LX-10 based on the experiments of Green *et al.*³⁶ Details of the friction model and the coefficients are provided in Ref. 39. Fourier’s heat conduction model is coupled with mechanical deformation and failure models to account for thermal conduction in the material. Details of the algorithm and models can be found in Ref. 34. A brief outline of the constitutive and interfacial relations is given below.

The deviatoric part of the constitutive behavior of the HMX grains is described by an elasto-viscoplastic model. The specific form of the constitutive relation used is

$$\hat{\boldsymbol{\tau}}' = \mathbf{L} : (\mathbf{D}' - \mathbf{D}'_p), \quad (2)$$

where \mathbf{L} is the tensor of elastic moduli and $\hat{\boldsymbol{\tau}}'$ is the deviatoric part of the Jaumann rate of the Kirchhoff stress. For isotropic elastic response,

$$\mathbf{L} = 2\mu\tilde{\mathbf{I}} + \lambda\mathbf{I} \otimes \mathbf{I}. \quad (3)$$

Here, $\tilde{\mathbf{I}}$ is the fourth order identity tensor, λ and μ are Lamé’s first and second constants. \mathbf{D}' in Eq. (2) is the

deviatoric part of the rate of deformation, which can be decomposed into an elastic part and a viscoplastic part as

$$\mathbf{D}' = \mathbf{D}'_e + \mathbf{D}'_p, \quad (4)$$

where \mathbf{D}'_p is the viscoplastic part of \mathbf{D}' in the form of

$$\mathbf{D}'_p = \frac{3\dot{\bar{\epsilon}}}{2\bar{\sigma}} \boldsymbol{\tau}', \quad \text{with} \quad \bar{\sigma}^2 = \frac{3}{2} \boldsymbol{\tau}' : \boldsymbol{\tau}'. \quad (5)$$

Here, $\bar{\sigma}$ is the Misses equivalent stress, $\boldsymbol{\tau}'$ is the deviatoric part of the Kirchhoff stress, and $\dot{\bar{\epsilon}}$ is the equivalent plastic strain rate which has the form of

$$\left. \begin{aligned} \dot{\bar{\epsilon}} &= \frac{\dot{\bar{\epsilon}}_1 \dot{\bar{\epsilon}}_2}{\dot{\bar{\epsilon}}_1 + \dot{\bar{\epsilon}}_2}, \\ \dot{\bar{\epsilon}}_1 &= \dot{\bar{\epsilon}}_0 \left[\frac{\bar{\sigma}}{g(\bar{\epsilon}, T)} \right]^m, \\ \dot{\bar{\epsilon}}_2 &= \dot{\bar{\epsilon}}_m \exp[-a g(\bar{\epsilon}, T)], \\ g(\bar{\epsilon}, T) &= \sigma_0 \left(1 + \frac{\bar{\epsilon}}{\epsilon_0} \right)^N \left\{ 1 - \beta \left[\left(\frac{T}{T_0} \right)^\kappa - 1 \right] \right\}, \end{aligned} \right\} \quad (6)$$

where $\bar{\epsilon} = \int_0^t \dot{\bar{\epsilon}} dt$ is the equivalent plastic strain, $\dot{\bar{\epsilon}}_0$ and $\dot{\bar{\epsilon}}_m$ are reference strain rates, m and a are rate sensitivity parameters for strain rates below 10^3 s^{-1} and above $5 \times 10^4 \text{ s}^{-1}$, respectively, σ_0 is the quasi-static yield stress, ϵ_0 is a reference strain, N is the strain hardening exponent, T_0 is a reference temperature, and β and κ are thermal softening parameters. The function $g(\bar{\epsilon}, T)$ represents the quasi-static stress-strain response at ambient temperature. The above relations consider strain hardening and strain-rate dependence of plasticity. The details of the above constitutive relations and descriptions of the parameters can be found in Ref. 40. The values of the parameters for HMX used in this study are listed in Table III. The parameters are calibrated to match the experimental wave profile obtained by Dick *et al.*⁴¹ The verification of the calibrated parameters is described in Ref. 32.

The volumetric part of the response is described by the Birch-Murnaghan equation of state (B-M EOS). The specific form of the equation is

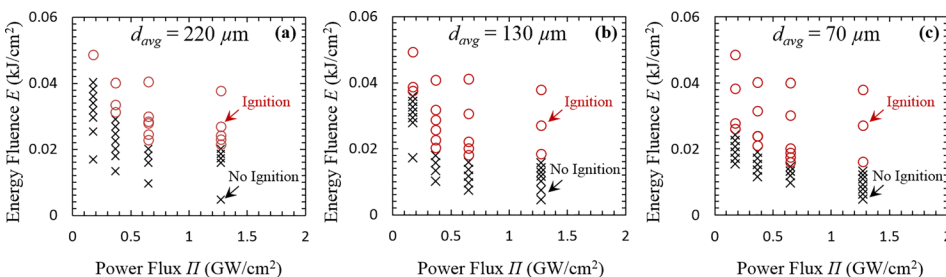


FIG. 6. Ignition threshold determination from computation using one microstructure of each grain size: (a) $d_{avg} = 220 \mu\text{m}$, (b) $d_{avg} = 130 \mu\text{m}$, and (c) $d_{avg} = 70 \mu\text{m}$. Multiple pulse durations are used for each load intensity.

TABLE III. Parameters in viscoplastic constitutive model of HMX.

σ_0 (MPa)	ε_0	N	T_0 (K)	β
260	5.88×10^{-4}	0.0	293	0.0
$\dot{\varepsilon}_0$ (s ⁻¹)	M	$\dot{\varepsilon}_m$ (s ⁻¹)	a (1/MPa)	κ
1×10^{-4}	100.0	8.0×10^{12}	22.5	0.0

$$\tau_h = \frac{3}{2} K_0 \left(\frac{dV}{dV_0} \right) \left\{ \left(\frac{dV}{dV_0} \right)^{-\frac{7}{3}} - \left(\frac{dV}{dV_0} \right)^{-\frac{5}{3}} \right\} \times \left[1 + \frac{3}{4} (K'_0 - 4) \left\{ \left(\frac{dV}{dV_0} \right)^{-\frac{2}{3}} - 1 \right\} \right], \quad (7)$$

where $\tau_h = \tau_{ii} = \tau_{11} + \tau_{22} + \tau_{33}$ is the hydrostatic part of the Kirchoff stress which is the product of the Jacobian and the negative of the hydrostatic pressure. K_0 is the bulk modulus and $K'_0 = (\partial K_0 / \partial P)_{P=0}$. dV/dV_0 is the volume ratio of an initial volume element (dV_0) and the current volume element (dV), which is equal to the Jacobian ($J = \det(\mathbf{F})$ with \mathbf{F} being the deformation gradient). For the implementation of the B-M EOS, a time incremental form is used. The time rate of change of the Jacobian is

$$\frac{\partial}{\partial t} \left(\frac{dV}{dV_0} \right) = \left(\frac{dV}{dV_0} \right) \text{tr}(\mathbf{D}) \quad (8)$$

and the rate of change of the hydrostatic Kirchoff stress is a function of the Jacobian and rate of deformation, i.e.,

$$\frac{\partial \tau_h}{\partial t} = f \left(\frac{dV}{dV_0}, \text{tr}(\mathbf{D}) \right). \quad (9)$$

Previous studies^{42–44} show the discrepancies in the parameters of B-M EOS for HMX. Landerville *et al.*⁴⁴ reported that the parameters vary to a large degree among experiments due to inherent noise of experiments and inconsistencies in fitting ranges and schemes. The parameter values used in this study are $K_0 = 16.71$ GPa and $K'_0 = 7.79$ as reported in Ref. 44 which lie in between the values of Gump

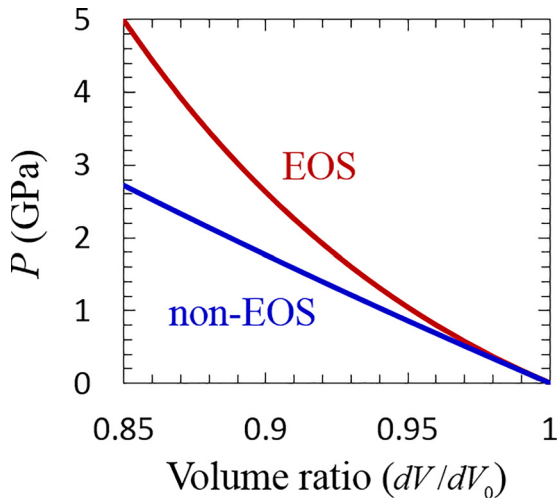


FIG. 7. Pressure–volume relations with the Birch-Murnaghan EOS and without the EOS.

and Peiris⁴² and Yoo and Cynn⁴³ Figure 7 shows the pressure–volume relations from models with and without the B-M EOS.

An artificial viscosity scheme is implemented to obtain stable shock response under high-intensity loading. The artificial viscosity is a commonly used practical approach to solve the issues associated with overshoot of stress at shock wave fronts and spurious oscillations behind the front. von Neumann and Richtmyer⁴⁵ first introduced the artificial viscosity method with a quadratic term of velocity gradient for 1-D wave propagations. Later, Landshoff⁴⁶ proposed a linear term for the velocity gradient. Campbell and Vignjevic⁴⁷ explained the effect of each term. The specific form used in this study is

$$q = \begin{cases} \rho c_L l a \{ \text{tr}(\mathbf{D}) \} - \rho c_Q l^2 \{ \text{tr}(\mathbf{D}) \}^2, & \text{if } \text{tr}(\mathbf{D}) < 0; \\ 0, & \text{if } \text{tr}(\mathbf{D}) \geq 0. \end{cases} \quad (10)$$

In the above relations, q is a pressure correction associated with the artificial viscosity, ρ is the mass density of the material, l is a characteristic grid length taken as the square root of the element area (\sqrt{A}), and $\text{tr}(\mathbf{D}) = D_{11} + D_{22} + D_{33}$ is the trace of the rate of deformation tensor. c_L and c_Q are viscous parameters for the linear term and the quadratic term, respectively. The values are $c_L = 0.06$ and $c_Q = 1.5$, as reported in Ref. 48. A material with behavior described by the elasto-viscoplastic model under shock loading shows less significant overshoot and oscillations of stress compared with a material with elastic behavior due to energy dissipation associated with plastic deformation. We carried out stability analyses not only for the conditions of viscoplasticity but also for the conditions of the more challenging elasticity. Figure 8 shows a comparison between the pressure profiles of a shock wave with artificial viscosity and without artificial viscosity for an elastic model of HMX under loading with $U_P = 400$ m/s. The algorithm with the artificial viscosity allows stable shock profiles without stress overshoot and spurious oscillations to be obtained. The introduction of an artificial viscosity may lower the shock velocity. Therefore, the parameters need to be calibrated such that the effect of the artificial viscosity on the shock velocity is negligible. To verify the implementation of the B-M EOS along with the artificial viscosity, the calculated Hugoniot or relation between shock velocity and particle velocity ($U_S - U_P$) is compared to that from experiments,⁴⁹ as shown in Fig. 9. The black dotted line is from the analytical solution of B-M EOS, and the red dots are from CFEM calculations with the B-M EOS and the artificial viscosity. A slight decrease in shock velocity from the CFEM calculations (red dots) is seen as compared to the analytically obtained shock velocity from the B-M EOS (black line), but the difference is negligible. The numerical result agrees with the experimental data (blue marks).

Interfacial debonding and arbitrary fracture patterns are explicitly captured by the use of cohesive elements embedded throughout the finite element model. The cohesive elements follow a bilinear traction separation law described by Zhai *et al.*⁵⁰ The cohesive relation embodies an initial

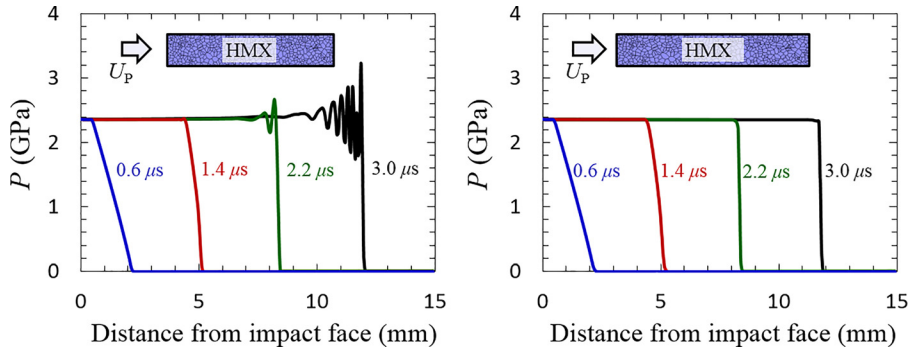


FIG. 8. Comparison between the pressure profiles of a shock wave: (a) without artificial viscosity and (b) with artificial viscosity for an elastic model of HMX under a shock intensity of $U_p = 400$ m/s.

reversible separation processes with a certain separation limit, followed by irreversible damage and separation beyond the limit. A cohesive surface pair is considered as failure and, therefore, has no further tensile strength if the separation reaches a critical distance. A verification of the cohesive element framework is provided in Ref. 34.

The formation of a crack (inside a grain or along a grain boundary) results in the creation of two surfaces. At each computational time step, the entire domain is scanned and such surfaces are identified. The corresponding nodal coordinates of all possible pairs of surfaces are compared to detect surface contact and overlap. Penalty forces are applied to strongly discourage interpenetration and maintain proper contact of the surfaces. Detailed descriptions of the multi-step contact algorithm and the penalty forces are given in Ref. 32. Frictional heating due to sliding along the surfaces in contact is assessed using the Coulomb friction law. The stick-slip state is determined by the normal force between the contact surface pairs.

Temperature in the material under dynamic loading rises locally due to inelastic bulk dissipation and frictional dissipation along interfaces. Heat conduction is considered. The specific form of the heat equation is

$$\rho c_v \frac{\partial T}{\partial t} = k \nabla^2 T + \eta \dot{W}^p + \dot{W}^{fric}, \quad (11)$$

where c_v is the specific heat, T is the temperature, t is the time, k is the thermal conductivity, η is the fraction of plastic

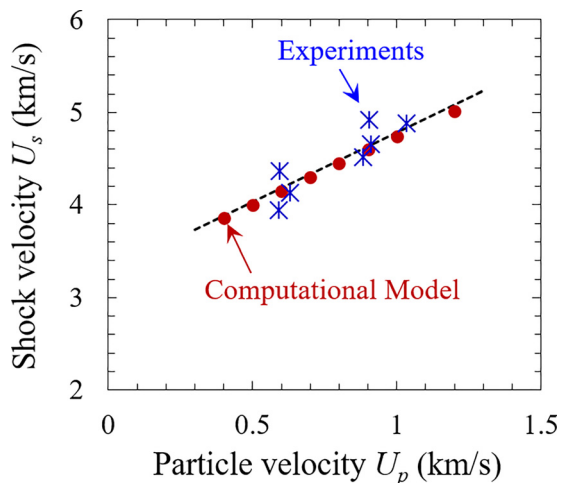


FIG. 9. Comparison of calculated Hugoniot ($U_s - U_p$ relation) and experimental data (Ref. 49) of HMX.

work that is converted into heat, \dot{W}^p is the rate of plastic work, and \dot{W}^{fric} is the rate of frictional dissipation.

D. Hotspot-based ignition criterion

The size and temperature of hotspots need to be quantified prior to the application of any threshold criteria for ignition. The temperature field of a sample from the CFEM calculation is scanned for localized temperature rises above a given temperature threshold (T_{thres}). Areas of a temperature field with temperatures above the threshold are analyzed for hotspots. Successively varying T_{thres} values allow the characteristics of a temperature field to be fully analyzed.

After all hotspots in a sample are quantified in terms of size and temperature, a recently developed criterion for ignition³⁵ is used to determine the onset of irreversible chemical decomposition of the HMX phase in the samples. This criterion provides a relationship between the size and the temperature states of critical hotspots. Specifically

$$d(T) \geq d_c(T), \quad (12)$$

where d is the diameter of a hotspot resulting from a loading event whose interior temperatures are at or above temperature T . d_c is the minimal diameter of a hotspot required for thermal runaway at temperature T . The quantitative information regarding the right-hand side of Eq. (12) is taken from the work of Tarver *et al.*⁵¹ who performed chemical kinetics calculations to analyze the criticality issue for HMX and TATB explosives. The calculations consider multistep reaction mechanisms and the pressure and temperature dependence of reactants and products. More details about the ignition criterion can be found in Ref. 35.

The left-hand side of Eq. (12) is obtained by analyzing the temperature fields in the microstructures from CFEM calculations. To account for the variations of temperature within a hotspot (note that temperatures at different spatial locations within a hotspot are different and the temperature threshold is the lowest temperature at the periphery), the hotspot threshold of Tarver *et al.* is treated as a band of $\pm 10\%$ about the mean value, as in Ref. 35. A hotspot is considered to be critical when it crosses the lower threshold limit (90% of the average value). The initiation of the material is regarded as being reached if the critical hotspot density is equal to or greater than 0.22 mm^{-2} which corresponds to two critical hotspots in a 3 mm square domain. The specific choice of the current critical hotspot density (0.22 mm^{-2}) is

based on the observation of Barua *et al.*³⁵ who observed a negligible difference on the criticality results by changing the critical hotspot density between 0.11 mm^{-2} (single hotspot in the whole sample) and 0.44 mm^{-2} (4 hotspots in the whole sample). This consistency is primarily because many hotspots develop simultaneously and reach the threshold within very short time intervals from each other. It has been contemplated that interactions among subcritical hotspots in close proximity of each other might lead to one critical hotspot or criticality. There has been no research on this subject. If a critical hotspot is to emerge from the interactions of multiple hotspots, it would be detected by the approach used here and accounted for by the ignition criterion. The possibility of multiple hotspots leading to ignition without first producing a critical hotspot, although not having been positively demonstrated, can be the subject of a future study.

To ensure timely execution and reasonable spatial resolution, the minimum element size used is $10 \mu\text{m}$. This is also the resolution for hotspot temperature fields. Convergence in mechanical response and local heating is obtained as the element size is below $15 \mu\text{m}$, as reported in Refs. 34 and 35. Therefore, the element size of $10 \mu\text{m}$ used in this study is adequate. The representative volume element (RVE) size is chosen based on the work of Liu *et al.*¹⁸ This treatment adequately addresses the RVE size issue with regard to the overall constitutive response of the material. The development of hotspots, inherently microstructurally dependent, can vary from one microstructure to another. Increasing the RVE size may slightly affect the criticality threshold due to randomness in microstructural heating. However, this issue is addressed by the use of a large number of statistically similar samples in each microstructure set. Finally, the model used is 2D. 3D microstructure models are more desirable but

are much more challenging when contact and friction need to be considered. At present, no such 3D model with all relevant physics exists. It will be the subject of future development.

E. Initiation vs. growth of reaction

This paper focuses on the establishment of ignition threshold associated with the development of critical hotspots. The analysis does not attempt to address the issue of growth to detonation transition that critical hotspots undergo. The model considers the attenuation of the shock wave as it travels through the sample, without considering the detonation waves from critical hotspots behind the shock front. This is quite reasonable in our opinion as the process leading up to the formation of critical hotspots does not involve detonation which occurs later. Since the relevant and dominant mechanisms of heat generation during this stage are mechanical irreversibilities (plastic deformation and fracture/friction), the only mechanism of heat loss from hotspots is thermal conduction which is accounted for in the model.

III. RESULTS AND DISCUSSION

A systematic quantification of the ignition of the HMX samples is carried out, focusing on the shock intensity, shock pulse duration, and the average grain size of the microstructure. The overall procedure is illustrated in Fig. 10. The analysis is performed in the following steps. First, three sets of microstructures with three average grain sizes are generated, with samples in each set having similar statistical attributes (e.g., average grain size and grain size distribution), as shown in Figs. 2 and 3. Second, CFEM calculations are carried out using the samples under the loading conditions as discussed in Sec. II B and

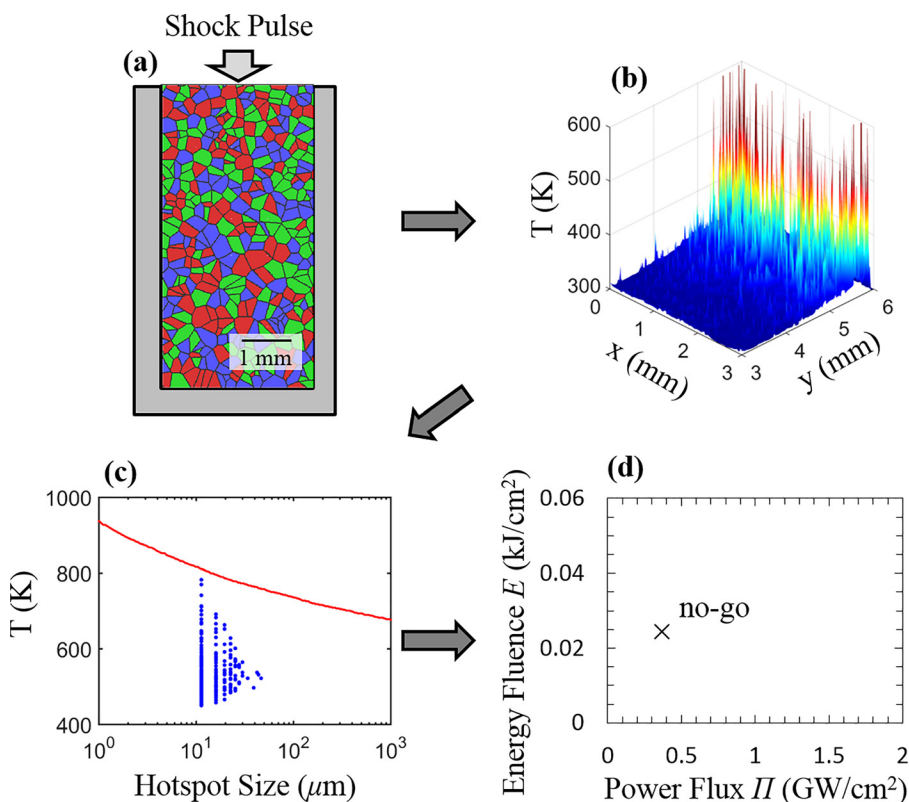


FIG. 10. Illustration of the hotspot-based approach for ignition threshold prediction. (a) Microstructure generation and CFEM simulation, (b) temperature field, (c) hotspot characterization from the temperature field and determination of the criticality of the sample via hotspot size-temperature states, and (d) determination of the “go” or “no-go” condition for each sample in the E – Π space.

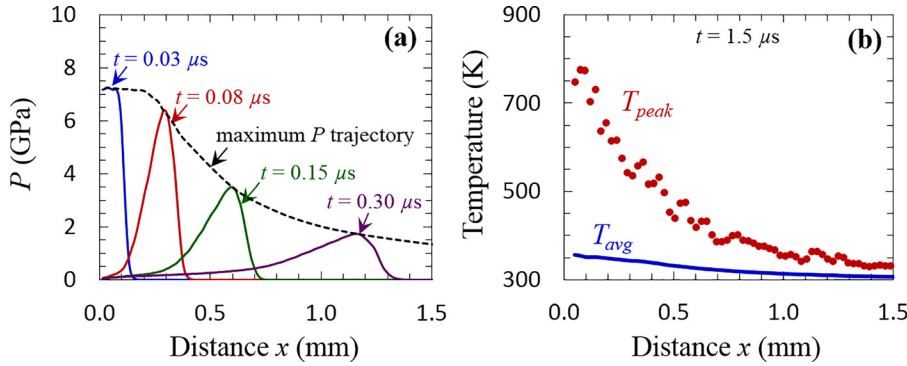


FIG. 11. (a) The calculated trajectory of peak pressure and (b) corresponding temperature profile under shock pulse loading with $U_p = 900$ m/s, $\tau = 38$ ns for a sample of $d_{avg} = 220$ μ m.

shown in Fig. 10(a). Temperature fields are obtained from the simulations as illustrated in Fig. 10(b). To ascertain the validity of the results relative to experiments, the attenuation of the stress waves as it traverses the samples is analyzed. Third, temperature fields and the size-temperature state of each hotspot are determined, as illustrated in Fig. 10(c). The ignition criterion described in Sec. II D is used to identify critical hotspots that have reached the size-temperature threshold. The ignition of the sample is determined by the existence of sufficient critical hotspots. Fourth, the ignition (go) or no ignition (no-go) condition in terms of the power flux and the energy fluence (measures for loading) for each sample is recorded, as illustrated in Fig. 10(d). The overall probability of ignition for each material set is determined using the aggregate data set of go-no go states of all samples in the power flux–energy fluence ($\Pi - E$) space. Detailed discussions on the probability of ignition will be given in Section III D.

A. Analysis of stress and temperature

The temperature of the material increases due to energy dissipation from material inelasticity and friction along crack faces under high stress. The dissipation also causes the shock wave to attenuate as it propagates. The peak pressure trajectory from the calculations and the corresponding temperature profile under loading with $U_p = 900$ m/s and $\tau = 38$ ns are shown in Fig. 11. Note that the peak pressure as well as the average and peak temperatures decrease spatially as the shock wave propagates into the material.

Impact by a thin flyer creates a short duration pulse, which attenuates as the shock wave propagates through the material, as described in Ref. 52. Initially, the peak pressure remains constant from the impact face to the rarefaction point

(x_c), after which release waves from the impact face overtake the shock wave, causing attenuation of the peak pressure. The distance (x_c) and the degree of attenuation vary depending on the material and initial pulse duration (which depends on flyer thickness), as described in Ref. 53. The attenuation of pressure is often quantified with an exponential form in terms of distance from the impact face, as discussed in Ref. 54. The exponential form has been shown to model the dependence of particle velocity (U_p) on the shock velocity (U_s).⁵⁵ The trajectories of peak pressure for different pulse durations between $\tau = 29 - 47$ ns are shown in Fig. 12(a). The trend can be described by

$$P_{peak} = P_1 \exp\left(-\frac{x - x_c}{x_r}\right) + P_2, \text{ for } x > x_c, \quad (13)$$

where the rarefaction point is at $x = x_c$ at which the peak pressure begins to attenuate. x_r is a scaling parameter that defines the slope of the attenuation. P_2 is the asymptotic pressure at far distances and $(P_1 + P_2)$ is the peak plateau pressure on the interval $0 \leq x \leq x_c$. The trajectories of the peak pressure as shown in Fig. 12(a) are fitted to Eq. (13) for the range of $x \leq 3$ mm. Figure 12(b) shows the dependence of x_r and x_c on pulse duration τ . As the pulse duration (τ) increases, the rarefaction distance (x_c) increases, indicating that the peak pressure plateaus for a longer distance before it starts to attenuate. Likewise, as the pulse duration (τ) increases, the distance scaling parameter (x_r) decreases, indicating that the pressure attenuates more slowly as it propagates through the material. Figure 13 shows the relationship between the pulse duration and the distance parameters (x_r and x_c) over the range of $U_p = 700 - 1200$ m/s. The relationships between the pulse duration and distance parameters,

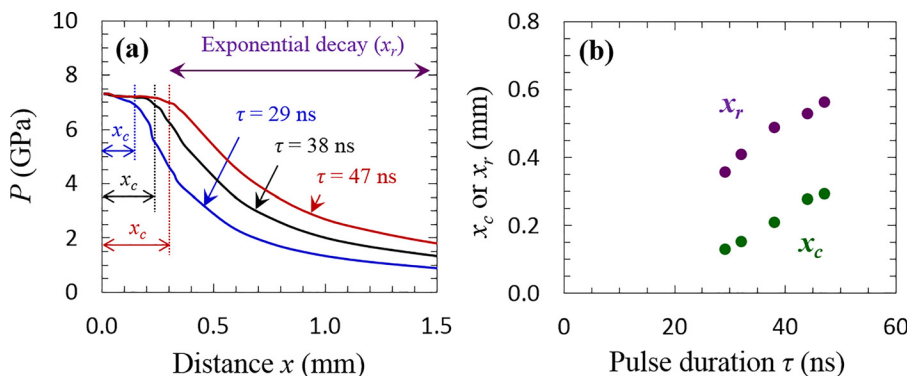


FIG. 12. Effect of pulse duration on stress attenuation under shock pulse loading with $U_p = 900$ m/s for a sample of $d_{avg} = 220$ μ m, (a) profiles of pressure for the durations of $\tau = 29, 38,$ and 47 ns and (b) corresponding rarefaction point (x_c) and decay distance scaling parameter (x_r).

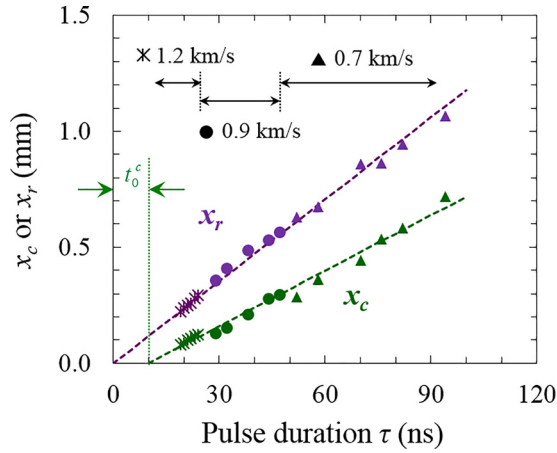


FIG. 13. Relationship between pulse duration and distance parameters (x_r and x_c) over the loading range of $U_p = 700\text{--}1200$ m/s.

x_r and x_c are linear. The distance parameters for all shock intensities considered fall along the same lines, indicating that they are highly dependent on pulse duration but are not strong functions of the load intensity. The effect of shock intensity on attenuation is captured by P_1 and P_2 . The values of the parameters for the linear relationships between pulse duration τ and the distance parameters, x_r and x_c , are listed in Table IV. The threshold time (t_0^c) for x_c in Figure 13 and Table IV is 10 ns which is equal to the ramp time of the applied boundary loading (Figure 5(b)). This coincidence indicates that if the pulse duration is as short as the ramp time, the shock wave begins to attenuate instantly without staying at plateau.

B. Ignition threshold

The samples in the experiments are 12.7 mm in length, which is a sufficient distance to see the stress attenuate to very low levels as the loading pulse reaches the bottom of the samples. The attenuation is so pronounced that only a small portion of the samples close to the impact face experience severe enough loading over the duration of the experiments to yield hotspots having the potential to cause ignition. Indeed, the computational results show that most hotspots are generated within a distance of $0 < x < 1\text{--}2$ times x_c from impact face, and no hotspots are seen for any distance $x > 4\text{--}5$ times of x_c . Therefore, the shock pressure significantly diminishes as the wave reaches $x = 6$ mm. Specifically, at this distance, the pressure of a sample subjected to loading with $U_p = 700$ m/s and $U_p = 900$ m/s decreases to 10% and 5% of the initial shock pressure, respectively. Welle *et al.*⁵⁶ investigated the effect of sample height and found no significant variations in the ignition threshold for a height range of 6–19 mm. Because of this, we stop our calculations when the stress wave reaches the bottom of the samples and analyze

TABLE IV. Coefficients of the linear relations between x_r and τ and between x_c and τ .

$x_r = a_r \cdot (\tau - t_0^r)$	$a_r = 0.0118$ mm/ns	$t_0^r = 0$ ns
$x_c = a_c \cdot (\tau - t_0^c)$	$a_c = 0.0080$ mm/ns	$t_0^c = 10$ ns

the temperature field for hotspots, knowing that further propagation and reflection of the wave from the bottom have negligible effects on hotspot formation. This approach is essentially equivalent to using an infinitely long sample in which the stress wave does not reflect.

The critical energy threshold for ignition is analyzed using the hotspot ignition criterion discussed in Sec. IID. Figure 14 shows the minimum energy input E required for ignition (or energy fluence). Five statistically equivalent samples are computationally analyzed at each energy input rate (or energy flux). The different samples, just like different samples of the same material in experiments, require slightly different levels of energy fluence (as reflected in slightly different pulse durations they require for reaching ignition) under the same load intensity or energy flux (energy input rate). Here, the shock intensity is expressed in a power flux form (i.e., $\Pi = P U_p$). Although the individual samples have the same overall statistical microstructural attributes therefore mimicking multiple samples of the same material batch in experiments, the random grain shapes and grain distributions cause the samples to have local fields that fluctuate, thereby giving rise to slightly different behaviors and slightly different energy fluence values even under the same overall loading condition. The asterisk in the figure demarcates the threshold for 50% probability of ignition as determined by all samples over the entire load regime analyzed. To determine this 50% threshold, the following James-type relation is used to provide an overall fit:

$$1 = \frac{E_c}{E} + \frac{\Pi_c}{\Pi}, \quad (14)$$

where the cutoff energy fluence E_c and the cutoff power flux Π_c are fitting parameters which represent asymptotic thresholds for the critical energy fluence and the critical power flux, respectively. This relation is based on the James relation² and is obtained by replacing the specific kinetic energy ($\Sigma = 0.5 U_p^2$) in the James relation by the power flux ($\Pi = P U_p$), see Welle *et al.*²³ The data points above the 50% threshold curve correspond to ignition probabilities higher than 50%, and the points below the 50% threshold

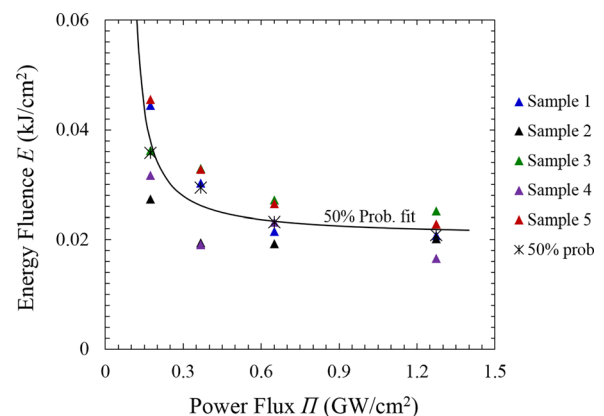


FIG. 14. Minimum energy required for ignition from five samples and 50% probability. The samples used here have statistically similar microstructures with the average grain size of $d_{avg} = 220$ μm as shown in Fig. 3.

curve represent correspond to ignition probabilities lower than 50%.

The 50% ignition thresholds for the three materials with the average grain sizes of $d_{avg} = 70, 130,$ and $220 \mu\text{m}$ are shown in Fig. 15. The corresponding parameters for the modified James relation (Eq. (14)) for these three cases are listed in Table V. In general, a higher loading rate (power flux) results in a lower energy required for ignition (lower energy fluence) as indicated by Eq. (14). For a given loading rate (power flux), smaller grain sizes lead to lower ignition thresholds. This effect is more pronounced under strong shock loading (power flux greater than 0.5 GW/cm^2). Khasainov *et al.*⁵⁷ mentioned that heterogeneous explosives with high surface area (corresponding to smaller grains) are more sensitive than those with less surface area (corresponding to larger grains). They observed this trend only at high intensity regime ($P/P_c \gg 1$). As shown in Fig. 15, the discrepancy in the sensitivity levels of different grain sizes increases as the power flux increases, whereas the sensitivity level discrepancy converges as the power flux decreases until its critical value is reached. The trends observed in the computational predictions are in good agreement with those observed in experimental data, as overlaid in Fig. 15. Moreover, the computationally predicted thresholds for grain sizes of $d_{avg} = 70, 130,$ and $220 \mu\text{m}$ lie in the same range as the thresholds obtained by experiments for Class 3 ($d_{avg} = 360 \mu\text{m}$) and Class 5 ($d_{avg} = 6.7 \mu\text{m}$) samples with a marginal degree of deviation. Overall, the experimentally measured thresholds are lower than the computational predictions. The difference between the experimental observations and computational predictions may be attributed to the following factors. First, the average grain sizes for Class 3 and Class 5 HMX in the experiments become smaller during the pressing process. So, the actual grain sizes are somewhat smaller than the nominal values stated here. Molek *et al.*²² reported that the grain sizes of Class 3 and fluid-energy-milled HMX ($d_{avg} = 4 \mu\text{m}$) decrease by roughly one or two orders of magnitude after sample preparation. Similar results can also be found in Ref. 58. Therefore, the ignition thresholds of Class 3 and Class 5 HMX shown in Fig. 15 are actually for grains sizes smaller than nominal values stated in the figure. Second, the computational model is based on a relative density of 100% (fully packed HMX) and provides only a phenomenological account of voids and other defects in the material, whereas the experimental samples have a

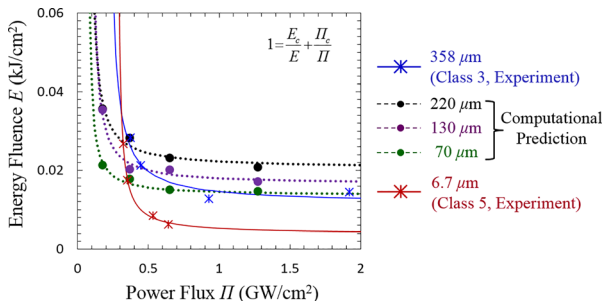


FIG. 15. Computationally predicted 50% ignition thresholds from all grain sizes analyzed ($d_{avg} = 70, 130,$ and $220 \mu\text{m}$) and experimentally measured thresholds for Class 3 and Class 5 HMX.

TABLE V. Parameters in the modified James relation for materials with different grain sizes from experiments and computations.

	$d_{avg} (\mu\text{m})$	$E_c (\text{kJ/cm}^2)$	$\Pi_c (\text{GW/cm}^2)$
Experiments	358 (Class 3)	0.01157	0.2072
	6.7 (Class 5)	0.00377	0.2776
Computations	220	0.0205	0.0798
	130	0.0163	0.0919
	70	0.0135	0.0683

relative density of less than 100% (94% TMD). Christensen *et al.*⁵⁹ observed that the LX-17 PBX samples with higher relative densities are less sensitive (having higher ignition thresholds) than the samples with lower relative densities. Third, large “boulders” in the experimental samples are not considered in the simulations, as pointed out earlier. What is important to note is that the overall trends are consistent, with smaller grain yielding lower ignition thresholds. Note that this sensitivity analysis does not account for subcritical hotspots. More information illustrating the effect of subcritical hotspots is presented in Sec. III D.

In the modified James relation (Eq. (14)), the power flux ($\Pi = P U_P$) is related to the shock intensity, similar to the specific kinetic energy ($\Sigma = 0.5 U_P^2$). It also represents the rate of energy imparted to the material ($\Pi = dE/dt$) per unit area of material surface. The ignition threshold between input energy E and power flux Π in the $E - \Pi$ space can also be represented in the $\Pi - \tau$ space. Specifically, the modified James relation as expressed in the $\Pi - \tau$ space is

$$\Pi = P \cdot U_P = \Pi_c \cdot \left(1 + \frac{E_c / \Pi_c}{\tau} \right), \quad (15)$$

where E_c and Π_c are the same parameters as in Eq. (14). This equation in the $\Pi - \tau$ space is an equivalent form of the modified James relation (Eq. (14)). The details of the derivation of the modified James relation and the equivalent modified James relation are given in Appendix. Figure 16 shows the 50% ignition thresholds (data points denoted by the symbols) for the three grain sizes in the $\Pi - \tau$ space and the corresponding equivalent James relations obtained via curve

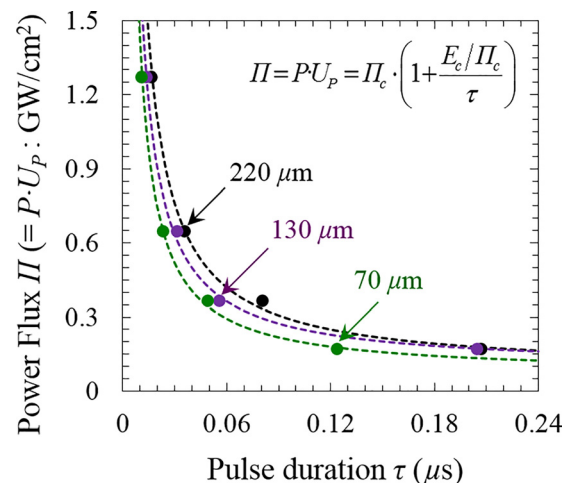


FIG. 16. Fifty percent (50%) ignition probability thresholds in the $\Pi - \tau$ space and the equivalent James relation.

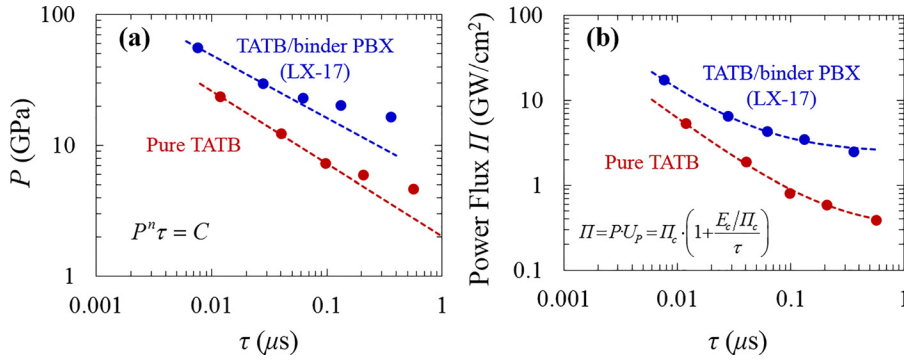


FIG. 17. Comparison of the ignition threshold characterizations using (a) the Walker-Wasley relation ($P^n \tau = C$) and (b) the equivalent James relation. The ignition data of LX-17 and TATB is from Ref. 60.

fitting. To study the application of the equivalent James relation to experimental data, we examine the shock initiation threshold of TATB obtained by Honodel *et al.*⁶⁰ Figure 17 shows a comparison of the fits with the equivalent James relation (Eq. (15)) and the Walker-Wasley relation ($P^n \tau = C$).⁶¹ Both the Walker-Wasley relation and the equivalent James relation have two fitting parameters. The equivalent James relation more closely follows the data points over the entire range, while the Walker-Wasley relation deviates from the experiments in the longer pulse (lower load intensity) regime. The closeness of the fit in the $\Pi - \tau$ space using the equivalent James relation (Eq. (15)) is the same as the closeness of the fit in the $E - \Pi$ space using the modified James relation (Eq. (14)), because Eqs. (14) and (15) are algebraically equivalent. The difference is that the $\Pi - \tau$ space directly relates to the physical conditions of the experiments (thickness of the flyer required for ignition at a given flyer velocity implied by the energy flux), whereas the $E - \Pi$ space emphasizes the amount of energy required for ignition at a given energy input rate into the material.

C. Probabilistic quantification: Ignition threshold for any given probability of ignition

The ignition threshold represented by Eq. (14) indicates the shock loading conditions for 50% probability of ignition. To incorporate the energy and power flux conditions required for greater than or less than 50% ignition probability, Gresshoff and Hrousis⁴ expanded on the modified James relation by introducing a James number, J . The specific form of the equation is

$$\frac{1}{J} = \frac{E_c}{E} + \frac{\Pi_c}{\Pi}, \quad (16)$$

where $J = 1$ is the modified James relation, $J > 1$ corresponds to shock loading conditions resulting in greater than 50% ignition probability, and $J < 1$ corresponds to shock loading conditions resulting in less than 50% ignition probability. As an example of the application of Eq. (16), Figure 18 shows the modified James relation with $J = 0.75$, 1.0, and 1.25 using the data for microstructures with $d_{avg} = 220 \mu\text{m}$. Each J number accounts for all combinations of loading conditions (i.e., energy fluence and power flux) which results in a certain probability of ignition. The three lines in Fig. 18 for $J = 0.75$, 1.0, and 1.25 correspond to the three probability fits of 10%, 50%, and 90%, respectively.

Figure 19 shows the relationship between J (James number) and the ignition probability from the experiment and the computational prediction for all samples. The truncated normal probability distribution function ($\mathcal{P}(J)$) is used to fit the ignition probability around a mean value of $J = 1$. The specific form of the function is

$$\mathcal{P}(J) = \frac{\Phi(J) - \Phi(0)}{\Phi(\infty) - \Phi(0)}, \quad (17)$$

where $\Phi(J)$ is the cumulative normal probability distribution⁴ in the form of

$$\begin{aligned} \Phi(J) &= \frac{1}{\sigma\sqrt{2\pi}} \int_{-\infty}^J \exp\left[-\frac{(x-\mu)^2}{2\sigma^2}\right] dx \\ &= \frac{1}{2} \left[1 + \operatorname{erf}\left(\frac{J-\mu}{\sqrt{2}\sigma}\right) \right], \end{aligned} \quad (18)$$

where μ is the mean value and σ is the standard deviation. Note that $\Phi(\infty) = 1$. The parameters used to represent the ignition probability of the samples are listed in Table VI. By combining Eqs. (16)–(18), we can obtain a direct relation between the ignition probability \mathcal{P} and the shock loading condition parameters E and Π in the form of

$$\begin{aligned} \mathcal{P}(E, \Pi) &= \frac{1}{1 - \operatorname{erf}\left(-\frac{\mu}{\sqrt{2}\sigma}\right)} \left[\operatorname{erf}\left(\frac{E\Pi}{\sqrt{2}\sigma(\Pi E_c + E\Pi_c)} - \frac{\mu}{\sqrt{2}\sigma}\right) \right. \\ &\quad \left. - \operatorname{erf}\left(\frac{-\mu}{\sqrt{2}\sigma}\right) \right], \end{aligned} \quad (19)$$

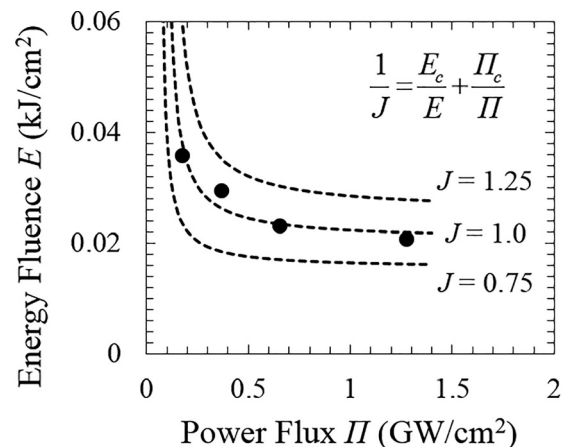


FIG. 18. Modified James relation with $J = 0.75$, 1.0, and 1.25 for the material with $d_{avg} = 220 \mu\text{m}$.

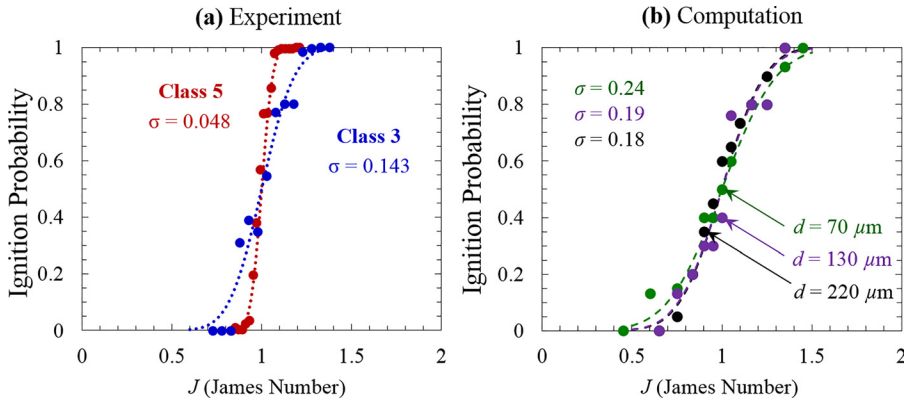


FIG. 19. Relationship between J and the ignition probability from (a) experimental results of Class 3 and Class 5 HMX and (b) computational results of grains sizes of $d_{avg} = 70, 130,$ and $220 \mu\text{m}$.

where $\text{erf}(\cdot)$ is the Gauss error function. Under the conditions of the current paper $\Phi(0) \approx 2 \times 10^{-5}$, therefore, for the range of $0 \leq J \leq \infty$, the difference between $\Phi(J)$ and $\mathcal{P}(J)$ is on the order of 2×10^{-5} , which is negligible. As a result, with $J = \mu = 1$ representing an ignition probability of 50%, Eq. (19) simplifies to

$$\mathcal{P}(E, \Pi) = \frac{1}{2} + \frac{1}{2} \text{erf} \left[\frac{1}{\sqrt{2}\sigma} \left(\frac{E\Pi}{\Pi E_c + E\Pi_c} - 1 \right) \right]. \quad (20)$$

In the above relations, the standard deviation σ , mean μ , cutoff energy fluence E_c , and cutoff power flux Π_c are material constants whose values are determined by experiments or computations reported here (see Tables V and VI). Once these parameters are determined for a material, the probability of ignition P under any loading condition as measured by E and Π can be calculated directly from Eq. (19) or (20). The probability P as a function of E and Π can also be represented as a function of the pulse duration τ and either power flux Π or input energy E . In Section III B, we have shown that the ignition threshold between input energy E and power flux Π in the $E - \Pi$ space can be represented in the $\Pi - \tau$ space (see Figs. 15 and 16). Similarly, the ignition probability P in Eq. (20) can be recast in the $\Pi - \tau$ space and in the $E - \tau$ space as, respectively,

$$\mathcal{P}(\Pi, \tau) = \frac{1}{2} + \frac{1}{2} \text{erf} \left[\frac{1}{\sqrt{2}\sigma} \left(\frac{\Pi/\Pi_c}{1 + \tau_c/\tau} - 1 \right) \right] \quad (21)$$

and

$$\mathcal{P}(E, \tau) = \frac{1}{2} + \frac{1}{2} \text{erf} \left[\frac{1}{\sqrt{2}\sigma} \left(\frac{E/E_c}{1 + \tau/\tau_c} - 1 \right) \right], \quad (22)$$

TABLE VI. Mean value and standard deviation for the ignition probability distributions for materials with different grain sizes from experiments and computations.

	$d_{avg} (\mu\text{m})$	μ	σ
Experiments	358 (Class 3)	1.0	0.143
	6.7 (Class 5)	1.0	0.048
Computations	220	1.0	0.18
	130	1.0	0.19
	70	1.0	0.24

where $\tau_c = E_c/\Pi_c$ is a material-dependent time-scale constant. The values of τ_c from experiments and computations are listed in Table VII. Note that although τ_c can be used as a reference time, it is not a measure related to the pulse duration required for ignition in any sense. For high-intensity loading, the pulse duration required for ignition τ can be smaller than τ_c . Likewise, for low-intensity loading, τ can be larger than τ_c .

The J -probability distribution for Class 3 samples from the experiments has a wider spread than that for the Class 5 samples, as shown in Fig. 19(a). This trend is consistent with what is reported by Schwarz^{3,62} who found that samples with lower specific interface areas (SIA) demonstrate a wider spread of ignition probability. The computational predictions for the three average grain sizes ($d_{avg} = 70, 130$ and $220 \mu\text{m}$) in Fig. 19(b) have similar J -probability distributions. The difference between the experimental and computational results may be attributed to the following factors. First, the grain size distribution of the experimental Class 5 samples is much wider than that of the Class 3 samples (see Table I in Ref. 56). On the other hand, the grain size distributions of the computational microstructures have the same spread (see Fig. 2). Second, the experimental samples have a much larger average grain size difference while the differences between the average grain sizes of the computational microstructure sets are much smaller. The difference between Class 3 and Class 5 is 53 times, whereas the differences among the computational sets are at most 3 times. The similarity in the distributions of ignition probability among the three computational sets does not mean that the average grain size does not significantly affect ignition. On the contrary, the average grain size significantly affects the ignition thresholds for all ignition probability levels (as seen in Section III B). For example, the thresholds for $J = 1$ (or 50% ignition probability) for the different grain sizes

TABLE VII. Time scale parameter τ_c obtained from experiments and computations.

	$d_{avg} (\mu\text{m})$	τ_c (ns)
Experiments	358 (Class 3)	55.8
	6.7 (Class 5)	13.6
Computations	220	257
	130	177
	70	198

are significantly different, as shown in Fig. 15 and by the parameters E_c and Π_c in Table V.

The distributions of ignition probability from the experiments have standard deviations of $\sigma = 0.048$ – 0.14 , and the calculated distributions have standard deviations of $\sigma = 0.18$ – 0.24 . As mentioned earlier, samples with larger specific interface areas (SIAs) result in narrower distributions of ignition probability. The experimental samples have much larger SIAs than the computational samples. Specifically, the SIAs of the computationally generated microstructures are 0.03 – $0.09 \text{ m}^2/\text{g} \pm 0.0014 \text{ m}^2/\text{g}$, one order of magnitude smaller than the SIAs of the samples used in the experiments (0.866 – $1.62 \text{ m}^2/\text{g}$).²³ One reason for this difference is that the computational samples do not explicitly resolve very small voids and defects inside the grains as well as the surface roughness of the grains. For example, the same order of magnitude of SIA with minimal roughness on surfaces of Al particles is attainable for average particle sizes of a few hundred nanometers (see Table I and the SEM images of Yarrington *et al.*⁶³). It is possible to explicitly consider these features in the model in the future, but such an analysis is beyond the scope of the current work, which focuses on a new method for predicting ignition thresholds. The differences in experimentally measured and theoretically calculated SIA are discussed by Sánchez *et al.*,⁶⁴ who compared the measured SIA values and theoretically obtained SIA values based on the particle size distributions. They reported that measured SIA values are an order of magnitude higher than theoretical SIA values due to particle morphology (roughness) and internal micro porosity.

Overall, the similarity in the distribution curves in Fig. 19 shows that (1) J serves as an effective normalizing parameter for the examination of the probability of ignition distribution around a given reference probability level (which is taken as $J = 1$ or 50% of ignition probability here) for samples with different microstructural attributes, and (2)

the ignition probability spread or the distribution around a given reference probability level depends on the microstructure heterogeneity fluctuations in the samples of a given sample set—or, simply put, how “similar to” or “different from” each other the multiple samples in a set are statistically. Specifically, the material-dependent 50% ignition threshold can be analyzed in the $E - \Pi$ space as seen in Fig. 15, and the ignition probability around this 50% threshold can be analyzed through the relation between J and the probability P given in Fig. 19. By combining these two relations, we can obtain the material-dependent ignition probability map as shown in Fig. 20. This process is equivalent to obtaining Eq. (20) by combining Eqs. (16) and (18). As Fig. 20 shows, the ignition probability level in the $E - \Pi$ space is highly dependent on microstructure.

D. Macroscopic and microscopic ignition risk factors

While J allows overall, macroscopic, material level ignition risk to be quantified, it is also possible and desirable to assess the ignition risk at the microscopic, individual sample level by studying its unique hotspot evolution. In the end, a relationship between the ignition of individual samples and the ignition risk of a material can emerge from such an analysis. To this end, we focus on the state of individual hotspots in a sample and introduce a quantitative measure to assess the risk for ignition of each individual hotspot, with the understanding that the most dominant hotspots with the highest risk factors determine the ignition risk of a sample. The specific risk factor we define here is the R -value, or “risk” value for an individual hotspot. It can also be referred to as the hotspot ignition risk determinant (HIRD) and depends on the proximity of a hotspot’s size-temperature state to the criticality condition embodied in Eq. (12). R is a measure for the proximity of a hotspot to the ignition threshold defined as

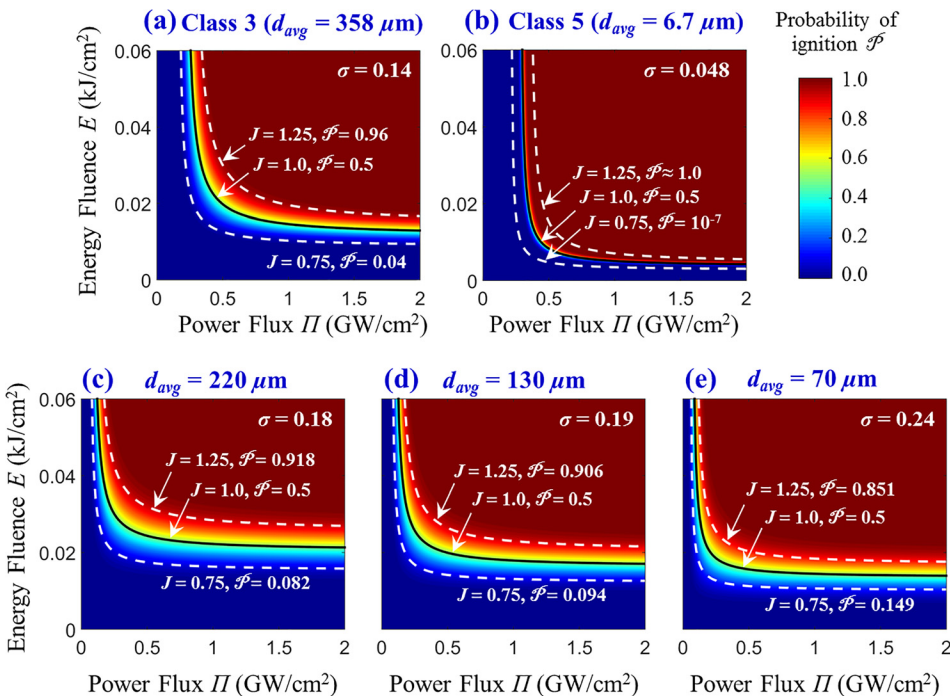


FIG. 20. Ignition probability distribution maps, ((a) and (b)) obtained from experiments for (a) Class 3 and (b) Class 5 pressed HMX, and ((c)–(e)) predicted from simulations for samples with (c) $d_{avg} = 220 \mu\text{m}$, (d) $d_{avg} = 130 \mu\text{m}$, and (e) $d_{avg} = 70 \mu\text{m}$. The vertical axes of all figures have the same scale and unit as shown in the left most plot in the top and bottom rows.

$$R = \frac{(T - T_i)}{(T_c - T_i)}, \quad (23)$$

where T is the temperature of a hotspot of diameter d , T_c is the critical threshold temperature for ignition for a hotspot of diameter d , and T_i is an initial reference temperature (chosen here as 300 K). Since the temperature and size combination of a hotspot depend on the area we choose to analyze (smaller cores of a hotspot have higher temperatures), the hotspot core size and R -value are calculated for different temperature levels (see Fig. 21—“Step 1”). The maximum value of R for each hotspot is taken as the R -value for that particular hotspot (Fig. 21—“Step 2”). This definition of R is a direct measure of how close a hotspot is to the ignition threshold. If $R = 0$, the hotspot is at the initial temperature ($T = T_i$) of the material at the beginning of loading. If $R = 1$, the hotspot is deemed critical ($T = T_c$) or has reached criticality (as defined in Sec. II D). Subcritical hotspots have $0 < R < 1$. The R value of a hotspot is the maximum value of R calculated using different cutoff temperatures in the analysis of the size-temperature state of that hotspot. The R -value allows hotspots to be grouped and analyzed via an R -curve, based on a histogram of all the R values for a sample. Figure 21 illustrates the number and states of critical and subcritical hotspots in a sample (see “Step 3”). It is important to note that $R > 1$ indicates hotspot states that are above the ignition threshold. Since the focus of the analysis here is only on the attainment of the threshold, such values are rounded down to

1 in the analysis carried out here. This treatment simply means that $R \geq 1$ indicates ignition, and since the ignition threshold is the sole concern here, no post ignition analysis is carried out.

Characterizing each sample with an R -curve makes it possible to compare the relative states of multiple samples in a holistic manner, accounting for the influence of all dominant hotspots. Figure 22 shows the average R -curves for the samples with the average grain sizes of $d_{avg} = 70, 130,$ and $220 \mu\text{m}$ under identical loading conditions ($U_p = 900 \text{ m/s}$ and $\tau = 35 \text{ ns}$). Each R -curve shows the average hotspot count of the five statistically similar samples in the set. The error bars show the extent of variations among the five samples. When compared to the experimental results for varying grain sizes, these R -curves demonstrate the correlation of hotspot quantity to overall sample sensitivity, which has been demonstrated to be related to the average grain size in Sec. III B. Samples with increased sensitivity to ignition are found to have a higher number of subcritical hotspots. In other words, for any given R value, the samples with lower average grain sizes have, on average, greater than or equal to the number of hotspots as samples with larger average grain sizes.

As a practical matter in the analysis reported here, in order to obtain a single R -value for each loading condition and sample, the average of the top two R -values in the sample is used. Two hotspots in the RVE correspond to a hotspot density of 0.22 mm^{-2} . Ten R -values are used for each

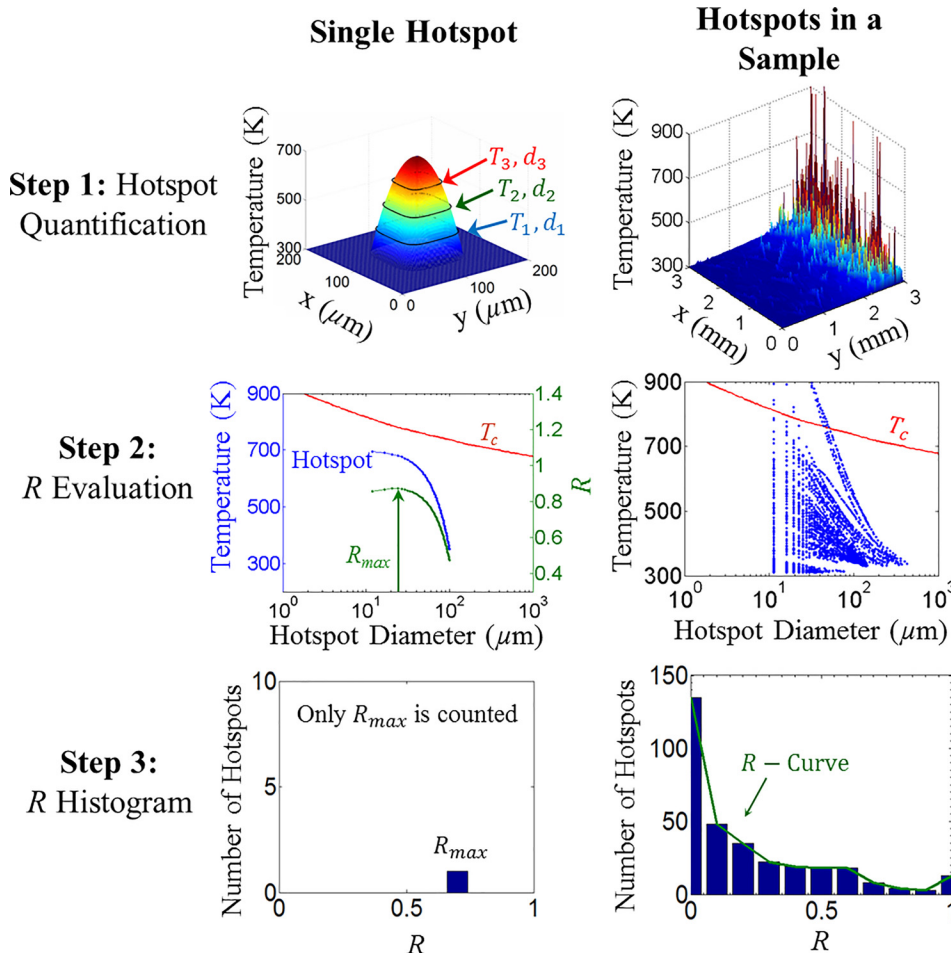


FIG. 21. Evaluation of R -value from a single hotspot and the R -curve from a temperature field.

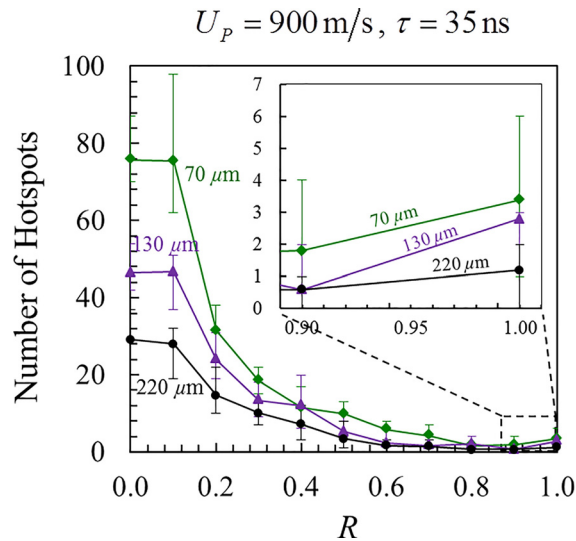


FIG. 22. Comparison of R -curves between sample sets with average grain sizes of $d_{avg} = 70, 130,$ and $220 \mu\text{m}$. The error bars indicate degree of variations among multiple samples in each material set.

loading condition: five samples and the highest two R -values per sample. Since $T_i = 300 \text{ K}$, $R = 0$ corresponds to $J = 0$. This makes intuitive sense because the only way for J to remain zero is if the sample has not been subjected to loading and no temperature increase is observed.

The R -value and R -curve focus on the local conditions of individual hotspots in a particular sample. Both the R -value and the J -value (discussed in Section III C) measure the likelihood of ignition. Note that for a given J value, some samples in a material set have ignited (with $R \geq J$), while other samples have not ignited (with $R < J$). For example, for $J = 1$ or an ignition probability of 0.5, 50% of all samples in a material set have reached criticality by definition (with $R \geq 1$) and 50% of the samples have not reached criticality (with $R < 1$). Therefore, R is inherently related to J with some statistical deviation due to microstructure stochasticity, reflecting the fact that J measures the aggregate statistical behavior of a material sample set and R measures the behavior of individual samples in the set. A practical difference between R and J is that R can be calculated from the outcome of a single simulation after analyzing the hotspot map of the sample, while J requires analyzing the results from multiple samples (experimentally or computationally). R can be used to predict and relate to the ignition probability of a material under given loading conditions. While J quantifies the result of this analysis and does not have the predictive

power or usage—its ability to “tell” or measure the ignition probability of a material only exists after the outcomes of a set of experiments or simulations have been analyzed and tabulated. Figure 23 shows the correlation between R and J and the 95% probability envelop for the three grain sizes. The standard deviation of the data points about $J = R$ in Fig. 23 is $\sigma = 0.17, 0.12,$ and 0.14 for the three cases, respectively. By studying the relationship between J and R , the inherent connection between loading conditions and hotspot development may be further understood. Since there is a strong correlation between R and J , it is possible to calculate the probability of ignition from a smaller number of samples without having to run a large number of tests or calculations to determine where the ignition threshold for $J = 1$ lies.

IV. CONCLUSION

The ignition thresholds of energetic materials have so far been exclusively determined through experiments. In this paper, we present a computational approach for predicating the James-type ignition thresholds via multiphysics simulations. The prediction does not involve calibration or curve fitting with respect to the predicted behavior (ignition threshold) nor does it require prior information about the predicted behavior. Rather, the prediction is based on material microstructural attributes and fundamental constituent as well as interfacial properties. The ignition thresholds are determined via an explicit analysis of the size and temperature states of hotspots in the materials and a hotspot based ignition criterion. The simulations consider the configuration and conditions of actual experiments. Specifically, the simulations account for the controlled loading of thin-flyer shock experiments with flyer velocities between 1.5 and 4.0 km/s on pressed granular HMX explosives with average grain sizes between $70 \mu\text{m}$ and $220 \mu\text{m}$. The choice reflects the interest in comparing the computational predictions with experimental results. James-type relations between the energy flux and energy fluence for different probabilities of ignition are predicted. To this end, statistically similar microstructure sample sets are computationally generated based on the features of micrographs of materials used in actual experiments.

The results show that the grain size significantly affects the ignition sensitivity of the materials at higher energy fluxes, with smaller sizes leading to lower energy thresholds required for ignition. Specifically, the 50% ignition threshold of the material with an average grain size of $220 \mu\text{m}$ is approximately 1.4–1.6 times that of the material with an average grain size of $70 \mu\text{m}$ in terms of energy fluence. The

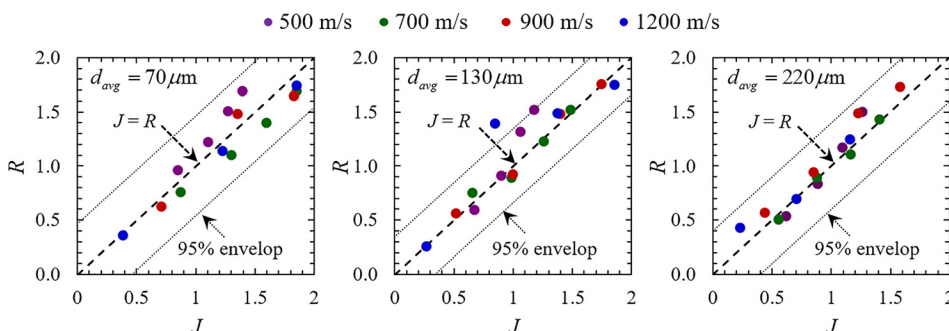


FIG. 23. Correlation between J and R for average grain sizes of $d_{avg} = 70, 130,$ and $220 \mu\text{m}$.

predicted thresholds are in general agreement with measurements from shock experiments in terms of trends. The statistical analysis on the ignition threshold leads to a probability-ignition map with respect to loading intensity and energy input. Once the material dependent parameters are determined, the probability of ignition under any loading condition can be calculated. This approach for the probability of ignition leads to the definition of a macroscopic ignition parameter J based on the loading conditions of the sample. A microscopic ignition risk parameter R is proposed based on the evolution of individual hotspots within the sample. The ignition risk parameter R represents the likelihood of ignition of individual hotspots at the microstructural-level, whereas the ignition parameter J concerns the loading intensities and energy input at the macroscopic level. The relationship between the two parameters is obtained. Specifically, it is found that R and J are strongly correlated ($J = R$) with some statistical deviations, reflecting the fact that J measures the aggregate statistical behavior of a material sample set and R measures the behavior of individual samples in the set.

This study has focused on pressed HMX only. However, the approach, relations, and capabilities developed here are useful for the analysis and design of heterogeneous energetic materials such as polymer-bonded explosives (PBX) and granular explosives in general. In particular, our next development is to apply this capability to PBX. Additionally, further development involves the application of microscopic ignition risk parameter R . It currently requires a significant number of runs to quantify J but only one to determine R for a single sample. Since the two parameters J and R are strongly correlated, the number of samples required to obtain the James type ignition threshold may be greatly reduced by analyzing the relationship between the R and J values. It must be pointed out that so far micropores have not been explicitly modelled, although their effects are to a degree indirectly implied via the weakening and variations of bulk material properties. The consideration of porosity is also a topic of interest for a future publication.

ACKNOWLEDGMENTS

The authors gratefully acknowledge the support from the Air Force Office of Scientific Research (Drs. Jennifer Jordan and Martin Schmidt) and the Defense Threat Reduction Agency (DTRA) (Drs. Douglas Allen Dalton and Suhithi Peiris). C. Miller acknowledges the support from the DoE NNSA Stewardship Science Graduate Fellowship Program (DENA0002135). The authors thank Dr. Ryan R. Wixom at Sandia National Laboratories for the SEM images in Fig. 1. Calculations are carried out on supercomputers at the ERDC and AFRL DSRCs of the U.S. DoD High Performance Computing Modernization Program. This article is approved for public release (Distribution A, 96TW-2016-0005).

APPENDIX: DERIVATION OF EQUIVALENT JAMES RELATION

Walker and Wasley⁶¹ introduced a shock initiation threshold based on the critical energy input of

$$E_{cr} = \frac{m_{fly} V_{fly}^2}{2}, \quad (A1)$$

where m_{fly} and V_{fly} are the mass and velocity of the flyer, respectively. For simplicity, assuming the impedance of the flyer is the same as the impedance of the sample, they used the following substitutions of variables:

$$\left. \begin{aligned} m_{fly} &= Aw\rho_{fly}, & \tau &= \frac{2w}{c_{fly}}, \\ V_{fly} &= 2U_p, & \text{and } U_p &= \frac{P}{\rho_{fly}c_{fly}} \end{aligned} \right\} \quad (A2)$$

where A is the area, w is the thickness, ρ_{fly} is the density of the flyer, and c_{fly} is the speed of the stress wave in the flyer. The pressure in the sample and flyer is denoted by P . Plugging the variables in Eq. (A2) into Eq. (A1) yields

$$P^2 \tau = \mu \frac{E_{cr}}{A} = \text{const.}, \quad (A3)$$

where μ is the impedance of the flyer ($\mu = \rho_{fly}c_{fly}$) which is assumed to be a constant. James² converted the $P - \tau$ relation to the $\Sigma - \tau$ relation in the form of

$$\Sigma = \frac{1}{2} U_p^2 = \frac{E_c}{2\mu\tau}, \quad (A4)$$

where E_c is critical energy fluence ($E_c = E_{cr}/A$) and Σ is specific kinetic energy ($\Sigma = 0.5 U_p^2$). To achieve a better representation of experimental data at low flyer velocities, James added an additional asymptotic line, denoted by Σ_c , which gives

$$\Sigma = \frac{E_c}{2\mu\tau} + \Sigma_c. \quad (A5)$$

Since $E = P U_p \tau$, Eq. (A5) can be represented as

$$1 = \frac{E_c}{E} + \frac{\Sigma_c}{\Sigma}. \quad (A6)$$

Welle *et al.*²³ replaced the specific kinetic energy ($\Sigma = 0.5 U_p^2$) by the power flux ($\Pi = P U_p$) to give

$$1 = \frac{E_c}{E} + \frac{\Pi_c}{\Pi}. \quad (A7)$$

Since the power flux ($\Pi = P U_p$) is the rate of energy imparted to the material ($\Pi = dE/dt$), we can eliminate the energy fluence and recast Eq. (A7) in the $\Pi - \tau$ space as

$$\Pi = \Pi_c \cdot \left(1 + \frac{E_c/\Pi_c}{\tau} \right). \quad (A8)$$

¹V. S. Solov'ev, "Some specific features of shock-wave initiation of explosives," *Combust. Explosion Shock Waves* **36**, 734–744 (2000).

²H. R. James, "An extension to the critical energy criterion used to predict shock initiation thresholds," *Propellants Explos. Pyrotech.* **21**, 8–13 (1996).

³A. C. Schwarz, "Study of factors which influence the shock-initiation sensitivity of hexanitrostilbene (HNS)," Sandia National Laboratories, Albuquerque, NM, USA, 1981, Report No. SANDBD-2372.

- ⁴M. Gresshoff and C. A. Hrousis, "Probabilistic shock threshold criterion," in Proceedings of the 14th International Detonation Symposium, Coeur d'Alene, ID, 2010.
- ⁵Y. Horie, "Hot spots, high explosives ignition, and material microstructure," *Mater. Sci. Forum* **767**, 3–12 (2014).
- ⁶M. R. Baer, "Modeling heterogeneous energetic materials at the meso-scale," *Thermochim. Acta* **384**, 351–367 (2002).
- ⁷E. L. Lee and C. M. Tarver, "Phenomenological model of shock initiation in heterogeneous explosives," *Phys. Fluids* **23**, 2362–2372 (1980).
- ⁸J. G. Bennett, K. S. Haberman, J. N. Johnson, and B. W. Asay, "A constitutive model for the non-shock ignition and mechanical response of high explosives," *J. Mech. Phys. Solids* **46**, 2303–2322 (1998).
- ⁹D. J. Benson and P. Conley, "Eulerian finite-element simulations of experimentally acquired HMX microstructures," *Modell. Simul. Mater. Sci. Eng.* **7**, 333–354 (1999).
- ¹⁰P. T. Rao and K. A. Gonthier, "Analysis of dissipation induced by successive planar shock loading of granular explosive," in Proceedings of the 51st AIAA/SAE/ASEE Joint Propulsion Conference, Orlando, FL, 2015.
- ¹¹R. A. Austin, N. R. Barton, J. E. Reaugh, and L. E. Fried, "Direct numerical simulation of shear localization and decomposition reactions in shock-loaded HMX crystal," *J. Appl. Phys.* **117**, 185902 (2015).
- ¹²M. M. Chaudhri, "Photographic evidence for ignition by friction in a deflagrating explosive single-crystal," *J. Phys. D: Appl. Phys.* **25**, 552–557 (1992).
- ¹³R. V. Browning and R. J. Scammon, "Microstructural model of ignition for time varying loading conditions," *AIP Conf. Proc.* **620**, 987–990 (2002).
- ¹⁴C. Gruau, D. Picart, R. Belmas, E. Bouton, F. Delmair-Sizes, J. Sabatier *et al.*, "Ignition of a confined high explosive under low velocity impact," *Int. J. Impact Eng.* **36**, 537–550 (2009).
- ¹⁵J. P. Curtis, A. G. Jones, C. T. Hughes, and J. E. Reaugh, "Modeling violent reaction following low speed impact on confined explosives," *AIP Conf. Proc.* **1426**, 669 (2012).
- ¹⁶A. Barua, Y. Horie, and M. Zhou, "Energy localization in HMX-Estane polymer-bonded explosives during impact loading," *J. Appl. Phys.* **111**, 054902 (2012).
- ¹⁷A. Barua, Y. Horie, and M. Zhou, "Microstructural level response of HMX-Estane polymer-bonded explosive under effects of transient stress waves," *Proc. R. Soc. London, Ser. A* **468**, 3725–3744 (2012).
- ¹⁸A. Barua and M. Zhou, "Computational analysis of temperature rises in microstructures of HMX-Estane PBXs," *Comput. Mech.* **52**, 151–159 (2013).
- ¹⁹H. R. James and B. D. Lambourn, "On the systematics of particle velocity histories in the shock-to-detonation transition regime," *J. Appl. Phys.* **100**, 084906 (2006).
- ²⁰A. G. Merzhanov and V. G. Abramov, "Thermal explosion of explosives and propellants. A review," *Propellants Explos. Pyrotech.* **6**, 130–148 (1981).
- ²¹B. D. Lambourn, H. J. Lacy, C. A. Handley, and H. R. James, "A simple model for the pressure field from a distribution of hotspots," *J. Phys.: Conf. Ser.* **500**, 052023 (2014).
- ²²C. D. Molek, E. J. Welle, R. R. Wixom, M. B. Ritchey, P. Samuels, and Y. Horie, "Microstructural characterization of pressed HMX material sets at differing densities," in Proceedings of the APS SCCM, Tampa, FL, 2015.
- ²³E. J. Welle, C. D. Molek, R. R. Wixom, and P. Samuels, "Microstructural effects on the ignition behavior of HMX," *J. Phys.: Conf. Ser.* **500**, 052049 (2014).
- ²⁴A. Barua, S. Kim, Y. Horie, and M. Zhou, "Prediction of probabilistic ignition behavior of polymer-bonded explosives from microstructural stochasticity," *J. Appl. Phys.* **113**, 184907 (2013).
- ²⁵W. Yan-Qing and H. Feng-Lei, "A micromechanical model for predicting combined damage of particles and interface debonding in PBX explosives," *Mech. Mater.* **41**, 27–47 (2009).
- ²⁶R. R. Wixom, A. S. Tappan, A. L. Brundage, R. Knepper, M. B. Ritchey, J. R. Michael *et al.*, "Characterization of pore morphology in molecular crystal explosives by focused ion-beam nanotomography," *J. Mater. Res.* **25**, 1362–1370 (2010).
- ²⁷X. Yang, T. Zhou, and C. Chen, "Effective elastic modulus and atomic stress concentration of single crystal nano-plate with void," *Comput. Mater. Sci.* **40**, 51–56 (2007).
- ²⁸R. J. Hudson, "Investigating the factors influencing RDX shock sensitivity," Ph.D. thesis, Applied Science and Engineering, Cranfield University, 2012.
- ²⁹R. J. Hudson, P. Zioupos, and P. P. Gill, "Investigating the mechanical properties of RDX crystals using nano-indentation," *Propellants Explos. Pyrotech.* **37**, 191–197 (2012).
- ³⁰T. D. Sewell, R. Menikoff, D. Bedrov, and G. D. Smith, "A molecular dynamics simulation study of elastic properties of HMX," *J. Chem. Phys.* **119**, 7417–7426 (2003).
- ³¹L. S. Dimas, D. Veneziano, T. Giesa, and M. J. Buehler, "Random bulk properties of heterogeneous rectangular blocks with lognormal Young's Modulus: Effective moduli," *J. Appl. Mech.* **82**, 011003 (2015).
- ³²D. B. Hardin, "The role of viscoplasticity in the deformation and ignition response of polymer bonded explosives," Doctor of Philosophy, Mechanical Engineering, Georgia Institute of Technology, 2015.
- ³³C. Liu, "On the minimum size of representative volume element: An experimental investigation," *Exp. Mech.* **45**, 238–243 (2005).
- ³⁴A. Barua and M. Zhou, "A Lagrangian framework for analyzing microstructural level response of polymer-bonded explosives," *Modell. Simul. Mater. Sci. Eng.* **19**, 055001 (2011).
- ³⁵A. Barua, S. Kim, Y. Horie, and M. Zhou, "Ignition criterion for heterogeneous energetic materials based on hotspot size-temperature threshold," *J. Appl. Phys.* **113**, 064906 (2013).
- ³⁶L. Green, A. Weston, and J. Van Velkinburg, "Mechanical and frictional behavior of skid test hemispherical billets," Lawrence Livermore Laboratory, California University, Livermore, 1971, Report No. UCRL-51085.
- ³⁷P. M. Dickson, G. R. Parker, L. B. Smilowitz, J. M. Zucker, and B. W. Asay, "Frictional heating and ignition of energetic materials," *AIP Conf. Proc.* **845**, 1057–1060 (2006).
- ³⁸S. Chidester, L. Green, and C. Lee, "A frictional work predictive method for the initiation of solid high explosives from low-pressure impacts," Lawrence Livermore National Laboratory, CA, USA, 1993, Report Number: UCRL-JC-114186. Available at <http://www.osti.gov/scitech/servlets/purl/10103000>.
- ³⁹A. Barua, "Mesoscale computational prediction and quantification of thermomechanical ignition behavior of polymer-bonded explosives (PBXs)," Ph.D. thesis, Mechanical Engineering, Georgia Institute of Technology, Atlanta, GA, 2013.
- ⁴⁰M. Zhou, A. Needleman, and R. J. Clifton, "Finite-element simulations of shear localization in plate impact," *J. Mech. Phys. Solids* **42**, 423–458 (1994).
- ⁴¹J. J. Dick, D. E. Hooks, R. Menikoff, and A. R. Martinez, "Elastic-plastic wave profiles in cyclotetramethylene tetranitramine crystals," *J. Appl. Phys.* **96**, 374–379 (2004).
- ⁴²J. C. Gump and S. M. Peiris, "Isothermal equations of state of beta octahydro-1,3,5,7-tetranitro-1,3,5,7-tetrazocine at high temperatures," *J. Appl. Phys.* **97**, 053513 (2005).
- ⁴³C.-S. Yoo and H. Cynn, "Equation of state, phase transition, decomposition of beta-HMX (octahydro-1,3,5,7-tetranitro-1,3,5,7-tetrazocine) at high pressures," *J. Chem. Phys.* **111**, 10229–10235 (1999).
- ⁴⁴A. C. Landerville, M. W. Conroy, M. M. Budzevich, Y. Lin, C. T. White, and I. I. Oleynik, "Equations of state for energetic materials from density functional theory with van der Waals, thermal, and zero-point energy corrections," *Appl. Phys. Lett.* **97**, 251908 (2010).
- ⁴⁵J. von Neumann and R. D. Richtmyer, "A method for the numerical calculation of hydrodynamic shocks," *J. Appl. Phys.* **21**, 232–237 (1950).
- ⁴⁶R. Landshoff, "A numerical method for treating fluid flow in the presence of shocks," DTIC Document 1955.
- ⁴⁷J. Campbell and R. Vignjevic, "Chap. 19 artificial viscosity methods for modelling shock wave propagation," *Predictive Modeling of Dynamic Processes* (Springer, 2009), pp. 349–365.
- ⁴⁸D. J. Benson, "Computational methods in Lagrangian and Eulerian hydrocodes," *Comput. Methods Appl. Mech. Eng.* **99**, 235–394 (1992).
- ⁴⁹R. L. Simpson, F. H. Helm, and J. W. Kury, "Non-reactive HMX shock hugoniot data," *Propellants Explos. Pyrotech.* **18**, 150–154 (1993).
- ⁵⁰J. Zhai, V. Tomar, and M. Zhou, "Micromechanical simulation of dynamic fracture using the cohesive finite element method," *J. Eng. Mater. Technol.* **126**, 179–191 (2004).
- ⁵¹C. M. Tarver, S. K. Chidester, and A. L. Nichols, "Critical conditions for impact- and shock-induced hot spots in solid explosives," *J. Phys. Chem.* **100**, 5794–5799 (1996).
- ⁵²A. Migault, "Concepts of shock waves," in *Impacts on Earth*, edited by D. Benet and C. Froeschlé (Springer, Berlin, Heidelberg, 1998), Vol. 505, pp. 79–112.
- ⁵³A. R. McMillan, W. M. Isbell, and A. H. Jones, "High pressure shock wave attenuation," General Motors, Virginia, Report No. DASA 2425, 1971.

- ⁵⁴C. Wall and M. Franson, "Validation of a pressed pentolite donor for the large scale gap test (LGST) at DSTO," Defence Science and Technology Organisation, Department of Defense, Australia, 2013, Accession Number: ADA576925, Document Number: DSTO-TN-1172. Available at: <http://www.dtic.mil/cgi-bin/GetTRDoc?Location=U2&doc=GetTRDoc.pdf&AD=ADA576925>.
- ⁵⁵R. Khurana, P. C. Gautam, R. Rai, A. Kumar, A. C. Sharma, and M. Singh, "Studies on shock attenuation in plastic materials and applications in detonation wave shaping," *J. Phys.: Conf. Ser.* **377**, 012051 (2012).
- ⁵⁶E. J. Welle, C. D. Molek, R. R. Wixom, P. Samuels, and J. Langhals, "Microstructure effects on the initiation threshold behavior of HMX and PBXN-5," in Proceedings of the 15th International Detonation Symposium, 2014.
- ⁵⁷B. A. Khasainov, B. S. Ermolaev, H. N. Presles, and P. Vidal, "On the effect of grain size on shock sensitivity of heterogeneous high explosives," *Shock Waves* **7**, 89–105 (1997).
- ⁵⁸N. J. Burnside, S. F. Son, B. W. Asay, and C. B. Skidmore, "Particle characterization of pressed granular HMX," *AIP Conf. Proc.* **429**, 571 (1997).
- ⁵⁹J. S. Christensen, M. Gresshoff, and K. J. McMullen, "Probabilistic shock threshold development for LX-17," in Proceedings of the 15th International Detonation Symposium, 2014.
- ⁶⁰C. Honodel, J. Humphrey, R. Weingart, R. Lee, and P. Kramer, "Shock initiation of TATB formulations," in Proceedings of the Seventh Symposium (International) on Detonation, Annapolis, Maryland, 1981, pp. 425–434.
- ⁶¹F. E. Walker and R. J. Wasley, "Critical energy for shock initiation of heterogeneous explosives," *Explosivstoffe* **17**, 9–13 (1969).
- ⁶²A. C. Schwarz, "Shock initiation sensitivity of hexanitrostilbene (HNS)," in Proceedings of the Seventh Symposium (International) on Detonation, Annapolis, Maryland, USA, 1981, pp. 1024–1028.
- ⁶³C. D. Yarrington, S. F. Son, T. J. Foley, S. J. Obrey, and A. N. Pacheco, "Nano aluminum energetics: The effect of synthesis method on morphology and combustion performance," *Propellants Explos. Pyrotech.* **36**, 551–557 (2011).
- ⁶⁴F. Sánchez, A. M. Bolarín, P. Molera, J. E. Mendoza, and M. Ocampo, "Relationship between particle size and manufacturing processing and sintered characteristics of iron powders," *Rev. Latinoam. Metal. Mater.* **23**, 35–40 (2003); available at: http://www.scielo.org.ve/scielo.php?script=sci_arttext&pid=S0255-69522003000100007&lng=en&nrm=iso&tlng=en.
- ⁶⁵C. M. May and C. M. Tarver, "Modeling short shock pulse duration initiation of LX-16 and LX-10 Charges," *AIP Conf. Proc.* **1195**, 275–278 (2009).